

Effect of Target Geometry on Ion Distributions from Laser-Produced Colliding Plasma Stagnation Layers

Columb B. Doherty

B. Sc.

A thesis submitted for the degree of:

Master of Science

Submitted to:

The School of Physical Sciences, Faculty of Science and Health,
Dublin City University

Research Supervisor

Prof. John T. Costello

July 2018

Declaration

I hereby certify that this material, which I now submit for assessment on the programme of study leading to the award of Master of Science is entirely my own work, that I have exercised reasonable care to ensure that the work is original and does not to the best of my knowledge breach any law of copyright and has not been taken from the work of others save and to the extent that such work has been cited and acknowledged within the text of my work.

Signed:

ID No.: 11349321

Date:

Acknowledgements

Firstly, and probably most importantly, I would like to thank my supervisor and mentor Prof. John Costello, for not only giving me the chance to carry out this research, but also for providing unending guidance and support along the way and helping me to develop as a researcher. I would also like to thank Dr. Mossy Kelly for sparking my interest in research and providing his time and tutelage since my undergraduate degree, as well as Dr. Tony Donnelly and Prof. James Lunney, for helping me get started with ESA experiments.

I want to thank Dr. Paddy Hayden for always being there to answer my questions, as basic as they may have been at times, and also all the others in our research group, specifically Ben and Steve, who would always take time from their own work to give me a hand.

I am eternally grateful to everyone in the physics department, especially Pat Wogan and Des Lavelle, without whom none of my work would have been possible, and who were always there for a friendly smile and a chat.

Finally I want to say thank you to my family and friends, and Malcolm, Mosey and Trisha most of all, for helping me to stay sane throughout.

Contents

Declaration.....	i
Acknowledgements.....	ii
List of Figures.....	iv
List of Tables.....	vi
Abstract.....	vii
1 Introduction.....	1
1.1 Plasma Definition.....	1
1.2 Previous Research.....	3
2 Theory.....	6
2.1 Laser-Produced Plasmas.....	6
2.1.1 Atomic Processes.....	8
2.1.2 Stagnation Layers.....	12
2.2 Ion Beams.....	13
3 Experimental Systems.....	15
3.1 Nd:YAG Laser System.....	18
3.1.1 Optics Setup.....	19
3.2 Energy Sector Analyser.....	21
3.2.1 Alignment.....	27
4 Results and Analysis.....	29
4.1 Initial Observations.....	29
4.2 Ion Signal Presentation and Analysis.....	34
5 Discussion.....	44
5.1 Summary of Findings.....	44
6 Conclusions and Future Work.....	47
References.....	49

List of Figures

Figure 1-1: Visualisation of the phase changes matter can undergo from a base state solid to an excited plasma [49]	1
Figure 1-2: A brief visualisation of the timeline of a laser plasma and stagnation layer formation.....	3
Figure 3-1: Schematic of the experimental setup featuring laser, optics, target and detector ...	15
Figure 3-2: Photograph of the experimental setup showing the laser, optics, vacuum chambers and some electrical and vacuum equipment. The optics setup consists of a half wave plate, polarizer, mirrors, neutral density filter, and on the second table a beam splitting wedge and focussing lens.....	16
Figure 3-3: Diagram of the Cu target used, featuring the 90°, 60° and 30° wedges for colliding plasmas (units in mm).....	17
Figure 3-4: Photograph of the ESA detector showing the curved Al plates, exit/entrance slits and electron multiplier for signal amplification.....	22
Figure 4-1: Comparison of the initial and smoothed ESA signals following application of the Savitzky-Golay filter. This signal shows the 1st charged state of Cu ⁺ from a colliding plasma on a flat Cu target at a plate bias of 75 V.....	29
Figure 4-2: Ion ToF signals for a single laser pulse, half a pulse and two colliding plasmas on a flat target.....	30
Figure 4-3: Ion ToF signals from colliding plasmas formed on 30°, 60° and 90° wedge targets.	31
Figure 4-4: Ion ToF signal of a single 73 mJ laser pulse on a 60° Cu target at a 75 V plate bias with CEM voltage of 1.668 kV	32
Figure 4-5: Ion ToF signal of a single 73 mJ laser pulse on a 180° Cu target at a 75 V plate bias with CEM voltage of 1.668 kV	32
Figure 4-6: Ion ToF signal from a 100 V biased ESA with fitted peaks to highlight the presence of ⁶³ Cu, ⁶⁵ Cu, ¹² C and ¹ H isotopes for each charged state as well as an initial laser photopeak.	34
Figure 4-7: Histogram of isotope signals at a plate bias of 50 V for a flat target for a single laser pulse, half the original laser pulse energy, and the original beam split in two for a colliding plasma	36
Figure 4-8: Histogram of isotope signals at a plate bias of 50 V for 3 different wedge targets – 90°, 60° and 30°	36
Figure 4-9: Histogram of isotope signals at a plate bias of 75 V for a flat target for a single laser pulse, half the original laser pulse energy, and the original beam split in two for a colliding plasma	37
Figure 4-10: Histogram of isotope signals at a plate bias of 75 V for 3 different wedge targets – 90°, 60° and 30°	37
Figure 4-11: Histogram of isotope signals at a plate bias of 100 V for a flat target for a single laser pulse, half the original laser pulse energy, and the original beam split in two for a colliding plasma	38
Figure 4-12: Histogram of isotope signals at a plate bias of 100 V for 3 different wedge targets – 90°, 60° and 30°	38
Figure 4-13: Histogram of isotope signals at a plate bias of 150 V for a flat target for a single laser pulse, half the original laser pulse energy, and the original beam split in two for a colliding plasma	39
Figure 4-14: Histogram of isotope signals at a plate bias of 150 V for 3 different wedge targets – 90°, 60° and 30°	39

Figure 4-15: Histogram of isotope signals at a plate bias of 200 V for a flat target for a single laser pulse, half the original laser pulse energy, and the original beam split in two for a colliding plasma 40

Figure 4-16: Histogram of isotope signals at a plate bias of 200 V for 3 different wedge targets – 90°, 60° and 30° 40

Figure 4-17: Kinetic energy distribution of ions from colliding plasmas formed on 90° and 180° wedge targets with a 50 V ESA bias 42

Figure 4-18: Kinetic energy distribution of ions from colliding plasmas formed on 90° and 180° wedge targets with a 100 V ESA bias 42

List of Tables

Table 3.1: Surelite Continuum Nd:YAG laser specifications	18
Table 3.2: Calculated Cu isotope ToF values at various plate biases for the first five ionisation stages.....	24
Table 3.3: Calculated C isotope ToF values at various plate biases for the first five ionisation stages.....	24
Table 3.4: Calculated H isotope ToF values at various plate biases	25
Table 3.5: ESA-ToF mass spectrometer dimensions	25
Table 3.6: Tabulated values of the calculated vs experimental ToF (μs) for isotopes from a flat target at a plate bias of 100 V, showing the average discrepancy in the ToF signal is $\sim 0.1 - 0.2 \mu\text{s}$	26
Table 3.7: List of the pass energies of ions in eV at the ΔV values used.....	27
Table 4.1: Tabulated values of the area under each isotope peak ($\text{V}^*\text{s}\times 10^{-6}$) at a 50 V plate bias	36
Table 4.2: Tabulated values of the area under each isotope peak ($\text{V}^*\text{s}\times 10^{-6}$) at a 75 V plate bias	37
Table 4.3: Tabulated values of the area under each isotope peak ($\text{V}^*\text{s}\times 10^{-6}$) at a 100 V plate bias	38
Table 4.4: Tabulated values of the area under each isotope peak ($\text{V}^*\text{s}\times 10^{-6}$) at a 150 V plate bias	39
Table 4.5: Tabulated values of the area under each isotope peak ($\text{V}^*\text{s}\times 10^{-6}$) at a 200 V plate bias	40

Abstract

When a laser pulse of sufficient intensity is focussed onto a flat metal target it vaporises the surface, forming a high temperature and high-density plasma that rapidly expands in a direction perpendicular to the target. If two laser-produced plasmas are created in close proximity to each other, upon expansion they collide and may, depending on density and relative velocity, either interpenetrate or stagnate along the collision front.

The purpose of this work is to investigate the ion emission characteristics of stagnation layers with a view towards developing a potential ion beam source for other research and commercial uses. This research aims to shed new light on the control that can be exercised over laser plasma generated ions, specifically with the use of colliding plasmas, and to explore how one can selectively alter the kinetic energy and charge state densities of the emitted ion beams.

This was investigated using mass spectrometry, with a particular focus on how the target geometry affects generation and distribution of highly charged ions over a range of kinetic energies. The work was carried out using an ESA-ToF MS (Energy Sector Analyser-Time of Flight Mass Spectrometer) device designed and built with assistance from the Laser and Plasma Applications Group in Trinity College Dublin. This detector was ultimately capable of isotope resolution for Cu ions with a minimum of background noise and could be tuned to examine kinetic energies of positively or negatively charged plasma species..

Using a colliding plasma system comprising two point plasmas focussed on a flat target, and a series of wedge shaped targets with angles of 90° , 60° and 30° , the ion emission was measured over a range of kinetic energies for each target. The results consistently show a visible increase in the proportion of highly ionised Cu atoms produced by using narrower wedge targets for every pass energy examined. On average there is a three-fold increase in the number density of higher charged states ($\text{Cu}^{3+,4+,5+}$) visible in the signal from a 90° target vs a 180° (flat) target. Concomitantly, there is a similar but smaller decrease in the percentage of lowly charged states in the 90° target signal.

1 Introduction

1.1 Plasma Definition

There exist four states of matter, arranged by thermal energies and intramolecular forces – solid, liquid, gas and plasma. In simple terms each successive phase change can be considered to be brought about by delivering more energy into the system, increasing the thermal vibrations of the atoms and, at high enough absorbed energy, even detaching electrons from individual atoms. In the lowest state of vibrational energy of a solid, the atoms are relatively static. An increase in thermal energy causes these structures to break down, leaving loose molecules which are still close together, but lack any regular structure or organization to them. This is the liquid phase, where molecules are free to vibrate and move past each other. Increasing the input energy further causes the molecules to agitate more vigorously, causing them to separate further into a gas [1]. Continuing to increase the supplied energy agitates the molecules further, eventually leading to fragmentation and electron emission yielding higher energy ions, electrons and radiation emissions. This is a plasma, defined primarily by its high temperature, charged particles and overall net electrical neutrality [2].

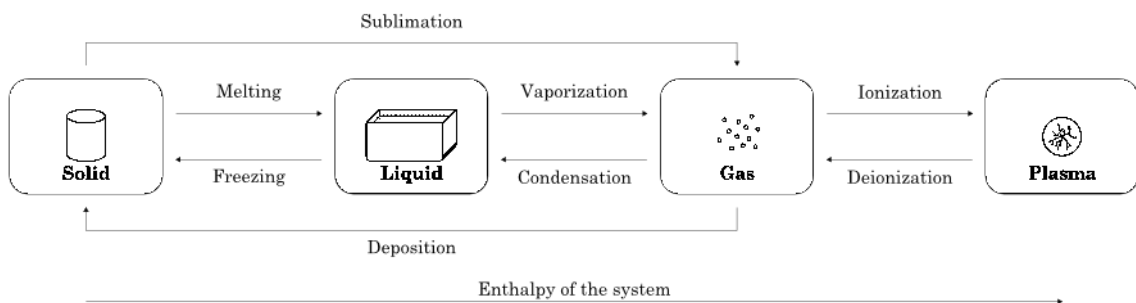


Figure 1-1: Visualisation of the phase changes matter can undergo from a base state solid to an excited plasma [50]

Initially described by Irving Langmuir in the 1920s, plasmas have long been the subject of intense research interest due to their unique characteristics and optical emission properties [3]. Laser produced plasmas are used in diverse fields such as pulsed laser

deposition, hohlraum targets for indirectly driven fusion, particle acceleration and laboratory-based astronomical simulations [4]–[7].

To meet the precise plasma classifications set forth it is required that the plasmas have an overall net neutrality of electrons and ions within the plasma such that:

$$n_e = \sum_z n_z z \quad (1.1)$$

where n_e is electron density and n_z is density of ions of charge z [8]. The plasma must also display a collective response to external forces due to the long-range Coulomb effect on charged particles within the plasma. The Debye length λ_D determines the maximum distance that the electric field of a charged particle can extend to before it is counterbalanced by the fields of other charged particles, and can be calculated from:

$$\lambda_D = \sqrt{\frac{\epsilon_0 k_B T}{n_e e^2}} \quad (1.2)$$

where ϵ_0 is the permittivity of free space, k_B is Boltzmann's constant, T is the plasma temperature and e is the electron charge. The plasma length L must be, at a minimum, an order of magnitude greater than the Debye length – this is to differentiate a true plasma from a highly energetic medium. Related to the Debye length is the concept of the Debye sphere, with a radius λ_D . Another requirement for plasma classification is that it must contain a sufficiently large number of particles stated as:

$$N_D = \frac{4\pi n_e}{3} \lambda_D^3 \gg 1 \quad (1.3)$$

where N_D represents of the average number of particles contained in a Debye sphere of radius λ_D . In the majority of plasmas an ion can only affect or be influenced by other ions within its Debye sphere.

1.2 Previous Research

This work builds upon previous research carried out in the areas of laser-produced plasmas, stagnation layers and ion analysis, going as far back as the 1960s when studies into PLA (Pulsed Laser Ablation) and LIBS (Laser Induced Breakdown Spectroscopy) initially began to garner interest [9].

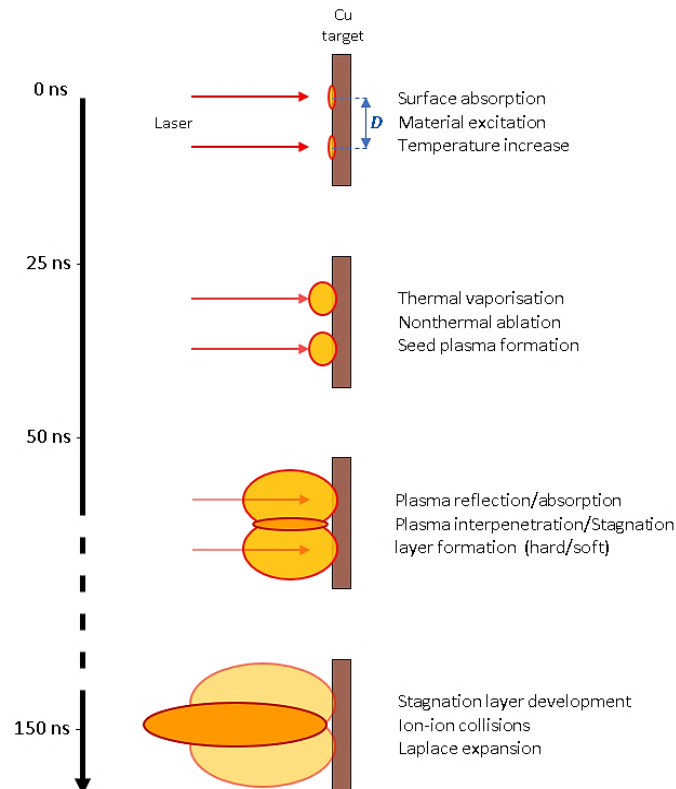


Figure 1-2: A brief visualisation of the timeline of a laser plasma and stagnation layer formation

There are several instances of groups examining laser-produced plasma stagnation layers using time, space and charge-resolved spectroscopy and imaging. The majority of these groups focussed on the photo-signal [10]–[12] whilst altering one or more variables of the plasma; a smaller number also examined the charged particle emissions using Faraday cups or mass spectrometry techniques [13]–[16]. The specific objectives of the research reported here relate to the generation and distribution of more highly charged ions (HCI) by manipulating the target geometry, endeavouring to increase the proportion of more HCIs relative to the generation of neutrals and lowly charged states.

In microelectronics HCIs with a large Coulomb potential energy are valued for their ability to reliably and significantly alter material surfaces and characteristics. HCIs are

used to remove electrons from a highly localized surface area of a material, forming hollow atoms where almost all electrons occupy excited levels leaving an empty central core, which can decay via Auger emissions. While this can be accomplished with more lowly charged ions (LCI) it is a difficult process, as rarely would a single particle possess sufficient energy to induce changes on its own – instead many particles are required to achieve what a single highly charged ion can potentially accomplish. This higher potential energy also allows the use of slower, low kinetic energy ions, making the generation and redirection of these ion beams easier [17].

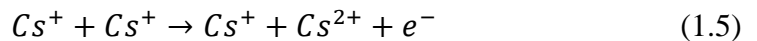
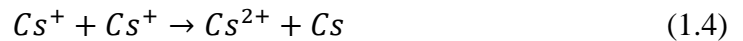
HCIs also play an important role in the biomedical field, specifically for cancer treatment. Hadron therapy enables doctors to target and destroy difficult to reach cancerous tumours, where surgical operations would be too risky or ineffective. This involves the generation, redirection and focussing of multiply charged particle beams to a minute focal point within the patient and can be used to target sensitive areas in the brain, prostate, lungs and other areas of the body. Using more slowly moving highly ionised particles for this purpose may be a simpler, more cost-effective method and, is potentially more potent than using a larger number of faster, lowly charged ions [18]. This treatment involves fewer, less severe side effects than conventional radiation treatments, meaning one can receive higher doses of radiation in each session with less risk of nearby tissue damage. This smaller number of more frequent higher intensity treatments, compared to conventional radiotherapy, can increase the likelihood of a positive clinical outcome for the patient.

The purpose of many previous studies on colliding plasmas was to verify to what extent the target and plume type affected the size, shape and emission characteristics of the stagnation layer to better characterize it for its various potential applications. Studies hypothesised that using narrower wedge shaped targets (as opposed to flat targets) would increase the relative collision velocity [19] (and thus the ion-ion mean free path (mfp)) as well as the width of the stagnation layer [15]. Using a target of greater atomic mass was also found to cause a significant increase in the width of the stagnation layer [20].

One of the earliest examples of a time of flight (ToF) mass spectrometer similar to the ESA (Energy Sector Analyser) used for these experiments is a design by Wiley and McLaren [21]. Their goal was to test the resolution of their improved electron gun, and

as part of this endeavour they designed their own mass spectrometer to aid them in their investigation. This design consisted of two collimating slits, a collimating magnetic field and an electron trap and electrodes. The slits help with beam collimation, the axial magnetic field further collimates the beam, the electron trap minimizes backscattering and the electrodes both accelerate the electrons and amplify the signal. This initial design has been modified in various ways since then to improve the resolution.

In 1985 Dolder et al. undertook the examination of two-body ion-ion collisions, reviewing previous publications on the experimental aspects of such collisions using intersecting ion beams [22]. Of note was their discussion on the mechanisms of ion collisions resulting in ionisation or charge transfer. Motivated by research into heavy ion fusion, experiments with identical ion pairs from Van de Graaff accelerator ion beams were carried out and yielded the following:



This fundamental reaction of intersecting ion beams somewhat mirrors the interactions that occur when a pair of plasmas collide but neglects the effect of the electron cloud. The investigation herein examines the change in charged states as the relative velocity is changed by altering the target geometry.

2 Theory

2.1 Laser-Produced Plasmas

Laser-produced plasmas are uniquely high energy short-lived plasma plumes (with lifetimes on the scale of 10 μs down to a few ps) created by a high energy photon pulse focussed onto a target, heating and ablating the surface to form a plasma. Photons from a high-powered laser pulse would typically lack the large amount of energy necessary to directly ionise matter and so ionisation is instead induced by a combination of fast electron collisions, multiphoton and/or field ionisation equation [23].

In experiments with Cu targets, the sample absorbs the laser energy resulting in electron heating, lattice heating and electron-phonon collisions [24]. The penetration depth of the laser pulse into the target surface can be calculated from the following [25]:

$$\delta = \sqrt{\frac{2}{\omega\mu\sigma}} \quad (2.1)$$

where δ is the penetration depth or optical skin depth (generally on a scale of several nanometres), ω is the angular frequency, μ is the magnetic permeability of free space and σ is the conductivity of the target material (measured in $\text{kg}^{-1} \text{m}^{-3} \text{s}^3 \text{A}^2$). The angular frequency ω also referred to as the laser oscillation frequency, can be calculated from:

$$\omega^2 = \omega_p^2 + c^2 k_p^2 \quad (2.2)$$

where ω represents the plasma frequency, c the speed of light in a vacuum and k_p is the propagation constant for the laser wave [26].

Using the values specific to the experiments carried out within this thesis, one obtains the following:

$$\delta_{Cu} = \sqrt{\frac{2}{2.818 \times 10^{14} \times 4\pi \times 10^{-7} \times 5.96 \times 10^7}} \quad (2.3)$$

$$\delta_{Cu} \approx 9.7 \times 10^{-9} \text{ m.}$$

Thus the optical skin depth for copper (using a 1064 nm wavelength at 20 °C) is calculated to be ≈ 9.7 nm.

This radiation is absorbed by electrons in the target material through photoexcitation, single photoionisation and multi-photon ionisation causing the release of free electrons [27]. These free electrons now travelling in the conduction band can transfer energy from the initial laser pulse into the bulk material. The depth to which this energy transfer can occur is described by L_{th} , the heat penetration depth:

$$L_{th} \approx \sqrt{2D\tau_L} \quad (2.4)$$

where τ_L is the laser pulse temporal duration and D represents the heat diffusion coefficient:

$$D = \frac{k}{\rho C} \quad (2.5)$$

wherein k is the thermal conductivity, ρ is the mass density, and C is the specific heat capacity of the target. With a heat penetration depth much larger than the optical skin depth, energy transfer from the laser pulse is mainly carried out through heat conduction deeper into the material, with the high energy input causing melting of the material. The vaporisation of the material can only occur when the energy absorbed by the optical skin depth exceeds the latent heat of evaporation of the target. The resulting ablation depth, ΔZ is calculated from:

$$\Delta Z \approx \frac{A_S(F_L - F_{th})}{\rho L_v} \quad (2.6)$$

where A_S is the surface absorbance, F_L is the laser fluence (J/cm^2), F_{th} is the threshold fluence and L_v is the latent heat per unit mass.

The heating within the ablation depth ΔZ causes the formation of what is known as a “deflagration layer”, formed from the electrons and ions released from the target surface. The impinging laser pulse interacts with the free electrons in this layer through the process of inverse bremsstrahlung (IB – bremsstrahlung being the German for “breaking radiation”). In this process, a laser photon is absorbed by an electron in the confines of the field of an ion of charge Z . This photo-absorption process depends greatly upon both the electron and ion densities as well as the laser pulse wavelength, resulting in the IB absorption coefficient described by:

$$\alpha_{IB} = \sigma_{IB} N_e = \frac{4}{3} \sqrt{\frac{2\pi}{3k_B T_e}} \times \frac{Z^2 e^6}{h c m_e^{\frac{2}{3}} v^3} n_i g_{ff} (1 - \exp(\frac{-h\nu}{k_B T_e})) n_e \quad (2.7)$$

where α_{IB} is the IB cross-section, n_i and n_e are the electron and ion density, ν is the laser frequency, Z is ion charge, h is Planck's constant, g_{ff} is the Gaunt factor [28][29].

The radiation absorption by IB imparts kinetic energy to the liberated electrons, causing further ionisation as the electron density increases. This process results in avalanche ionisation until the electron density reaches the critical value (which for a Nd:YAG operating at the fundamental frequency is $\sim 10^{21} \text{ cm}^{-3}$) at which point the plasma becomes opaque and the laser radiation is reflected from the critical density layer. This typically occurs during the first few tens of picoseconds. As the plasma expands out further the electron density decreases, descending below the critical density level, and radiation from the laser begins to be absorbed once again. This cycle repeats so long as the laser pulse continues to supply energy. This stage of the plasma evolution is primarily isothermal due to the actual expansion time greatly exceeding the heating cycle time. Through this phenomenon, the plasma is able to maintain a relatively constant temperature in the early expansion phase, even with the increasing plasma volume [30].

2.1.1 Atomic Processes

Within a laser-produced plasma there are multiple different radiative and collisional processes taking place that variously involve atoms, ions, electrons, other particles and diverse types of radiation to facilitate energy absorption, emission and transportation. Electron-electron collisions are generally the dominant particle interaction occurring within the plasma due to their high velocity, and while there are also many radiative processes that take place one is concerned here primarily with the ionisation and recombination processes triggered by ion-particle impacts, rather than the radiative processes. These are considered in more detail below.

2.1.1.1 Electron Impact Excitation

Electron impact excitation occurs when an electron travelling near an ion (within its Debye sphere of influence, determined by the Debye length λ_D in equation (1.2)) induces a bound electron transition through the transfer of some portion of its kinetic energy. This causes the free electron to lose energy equal to the energy difference between the upper (j) and lower (i) bound states.

2.1.1.2 Electron-Impact De-Excitation

This process is the inverse of electron-impact excitation and occurs when a free electron triggers the downward transition of a bound excited electron held by a nearby ion/atom to a lower bound state. The kinetic energy lost by the bound electron within the collision is converted into the increased kinetic energy of the free electron.

2.1.1.3 Electron-Impact Ionisation

Electron impact ionisation plays a particularly important role in low-density, optically thin plasmas, occurring at a much greater frequency than other processes. This describes the process whereby a free electron within the continuum collides with an atom/ion and transfers sufficient energy to a bound electron such that it may overcome its binding energy. This results in the electron being released and entering into the free electron continuum with an energy equal to that lost by the initial, colliding free electron, minus the ionisation energy.

2.1.1.4 Three-body Recombination

This process is the inverse of the previous electron-impact ionisation process and plays a more important role in high-density plasmas. When two separate free electrons enter the Debye sphere of influence of an ion simultaneously one of them may become captured into a bound state in the ion. The surplus energy of the now bound electron is transferred into an increase of kinetic energy of the second electron.

2.1.1.5 Photoionisation

Also known as the photoelectric effect, in this process a high energy photon is absorbed by an atom, causing the ionisation and promotion of a bound electron into the continuum. This plays a very important role in hot plasmas, but only when the incident photon energy is great enough to induce photoionisation on a scale comparable with the electron-impact ionisation in optically thick plasmas.

2.1.1.6 Radiative Recombination

This is the inverse process to photoionisation and is an important factor in high density plasmas. It occurs when a free electron in the continuum travels near an ion and becomes bound to it. This descent into a discrete bound state causes the emission of a photon of energy $h\nu$ and decreases the ionisation state of the ion by one. As the free electrons in a plasma exhibit a continuum of kinetic energies, the photons emitted also exhibit a continuum of energies and so this radiation is most often referred to as “recombination radiation” or recombination continuum.

2.1.1.7 Bremsstrahlung Radiation

This process occurs when a free electron passes through the electric field of an ion and is decelerated by the ion's Coulomb field (which is where the term originates from – “bremsstrahlung” being German for “braking radiation”). This decrease in the electron's kinetic energy within the electric field is balanced by the emission of a photon. This plays a major role in both low- z plasmas and highly ionised high- z plasmas, where z refers to the charge state or ionisation stage.

2.1.1.8 Inverse Bremsstrahlung Radiation

When a free electron travelling near an ion absorbs a photon it increases its kinetic energy by the amount of energy absorbed. For the conservation of momentum to be obeyed this process can only take place in the presence of an ion, which is needed to absorb the excess momentum.

2.1.1.9 Doubly Excited Auto-Ionisation

This process occurs only when there already exists an atom (or ion) with two electrons in high energy excited shells. An example is the $2s2p$ (1P) state in He with an excitation energy of 60.1 eV, well above the ionisation potential of He. These doubly excited electronic states are formed through resonant scattering of electrons or photons by atoms or ions and are clearly unstable tending to decay rapidly into a free electron and residual ion. In practice, one of the electrons drops to a lower (often ground) state and transfers its energy to the second electron which can then overcome the binding energy of the atom and is emitted into the continuum.

2.1.1.10 Dielectronic Recombination

When an electron is captured from the continuum to occupy an excited state in an ion of charge state z , the excess energy is released. This energy in turn promotes another lower electron into an upper excited state, resulting in a doubly excited atom (or ion) of charge state $z - 1$. This process is generally described as the inverse of the “autoionising” process.

2.1.2 Stagnation Layers

When two laser-produced plasmas are formed in close physical proximity they can collide and interact energetically, producing a unique energy/particle signature and can at one extreme (of plasma temperature and density) interpenetrate, or stagnate at the other extreme, or form some complex combination of both. They are typically formed in vacuo as this allows for the relatively uninhibited ballistic expansion of the plumes, decreasing the energy loss and recombination rates that would come with the increased collisions associated with a plasma formed in air.

Upon collision, if the plasmas are of low density and/or high relative velocity they will tend to interpenetrate, expanding into one another as the plasma constituents continue to undergo collisions. If the two plasmas are of high enough density and/or move at low relative velocity, they may stagnate upon collision [31]. This can be either a soft or hard stagnation: soft stagnation involves some degree of interpenetration while hard stagnation involves very little interpenetration. In this second case, the individual plasma constituents decelerate rapidly at the collision plane with the material here undergoing significant compression, causing a great increase in the temperature and density of the plasma at the collisional front (stagnation layer).

The factor that determines whether the plasmas will stagnate upon collision (and the degree of this stagnation) or interpenetrate is determined principally by the collisionality parameter, ζ :

$$\zeta = D/\lambda_{ii} \quad (2.8)$$

where D is the spatial separation between the two seed plasmas and λ_{ii} is the ion-ion mean free path (mfp), or the average distance between two ions within each plasma [32], which is itself defined as:

$$\lambda_{ii}(1 \rightarrow 2) = \frac{m_i^2 v_{12}^4}{4\pi q^4 z^4 n_i \ln \Lambda_{1 \rightarrow 2}} \quad (2.9)$$

where the indices 1 and 2 refer individually to the 1st and 2nd plasmas, m_i is the ion mass, v_{12} is the relative collision velocity, q is the fundamental electron charge, z is the average ionisation state of the plasma, n_i is the average ion density of the plasma and $\ln \Lambda_{1 \rightarrow 2}$ is the Coulomb logarithm (which denotes the natural log of collisions of the species from plasma 1 over the species from plasma 2 , revealing whether small- or large-angle collisions are more predominant in the plasmas [33]). When λ_{ii} is large there is a long ion-ion mfp, resulting in fewer collisions as the ions do not aggregate at the stagnation layer. When λ_{ii} is small the mfp is shorter, resulting in a higher number of collisions as the plasmas meet which creates a hard stagnation with little to no interpenetration of the expanding plumes.

Based on these equations one knows that to manipulate the stagnation layer, one can primarily control the distance D between the two plasmas, the relative collision velocity v_{12} of the initial plasmas or the mass m_i of the ion (by changing the target material). The work contained herein focusses largely on the manipulation of the target geometry (angle of incidence) and the effect of this upon the ion distribution (ion energies and ionisation balance) in the stagnation layer.

2.2 Ion Beams

By the time the plasma reaches the end of the detector, for all intents and purposes it resembles an ion beam (or at least a spatially extended ion bunch) consisting of various charge states and kinetic energies. The purpose of the drift tube is to allow these ions to spatially separate out from each other based on their degree of ionisation due to Coulomb field effects [34] and their kinetic energies. As the ions travel from the target

towards the detector along the drift tube the individual kinetic energies of ions belonging to each charge state causes the following separation:

$$t_z = \frac{D_{tube}}{v_z} \quad (2.10)$$

Where t_z refers to the time it takes for an ion to travel through the tube, z is the individual charge state (unless an electrical bias is applied to the tube) D_{tube} is the tube length and v_z is the ion velocity for each charge state.

The ions are then separated further in terms of kinetic energy by the applied electrical bias across the ESA's curved plates. The properties of this ion beam can be varied based on the formation of the laser-produced plasma, principally by altering either the laser fluence and spot size, or by altering the target geometry or material. To achieve high spatial separation, one can make use of targets with a high atomic mass and few charge states or increase the drift tube length, which gives the ions more time to separate spatially due to Coulomb field effects as the plasma expands towards the detector.

3 Experimental Systems

Analysis of the charge state energy distributions from the plasma was made possible with the aid of the ESA and drift tube length, forming an Energy Sector Analyser-Time of Flight Mass Spectrometer system (ESA-ToF MS) [25].

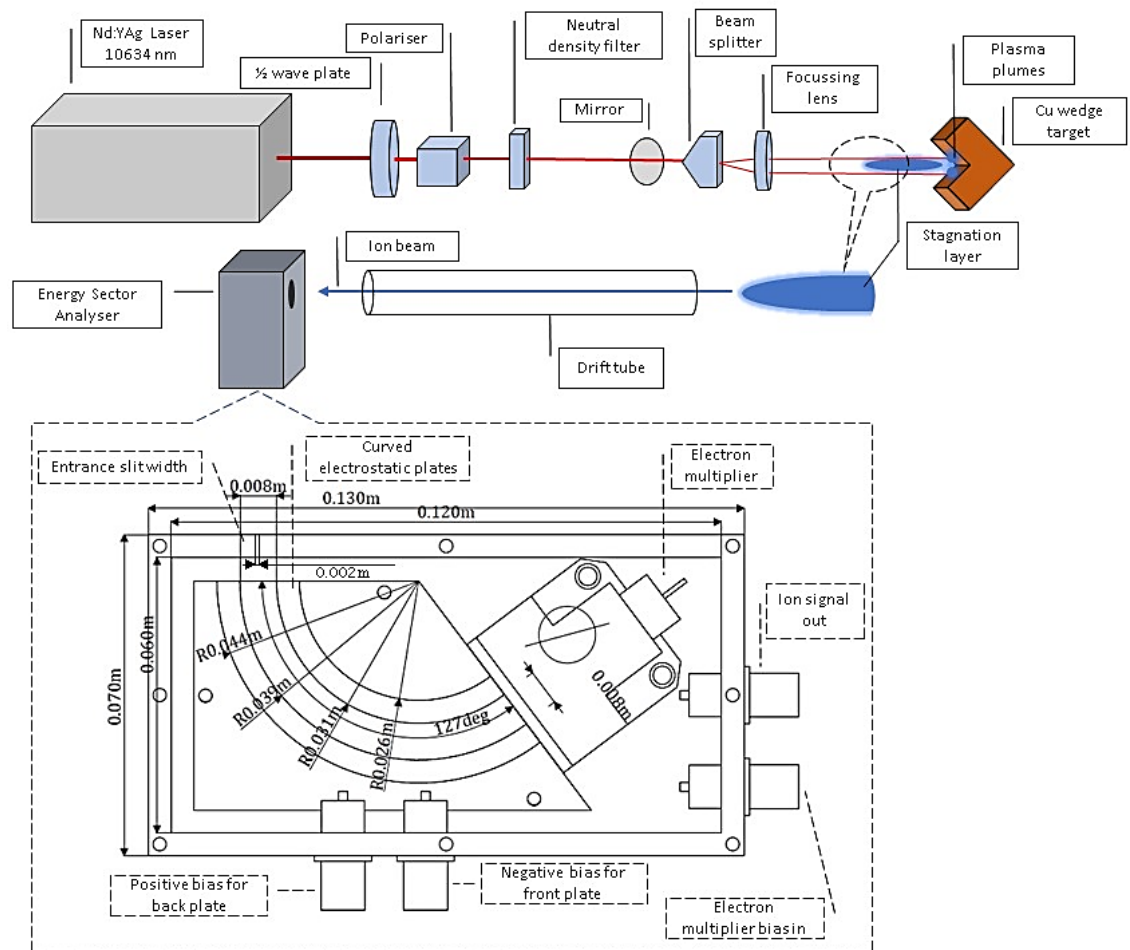


Figure 3-1: Schematic of the experimental setup featuring laser, optics, target and detector

Figure 3.1 shows the key components of the system, consisting of the laser, optical apparatus (for the redirection, attenuation and splitting of the laser beam), target and detector. The last two of these components are housed within the vacuum chambers at low pressures to allow for plasma expansion and detector functionality.

The low pressure (10^{-6} mbar) prevents ions from undergoing a large number of collisions with air molecules and any impurities in the air, which would result in a high

recombination rate and low signal at the detector. The low system pressure is also extremely important for the function of the electron multiplier within the ESA (Analytical West electron multiplier small horn plug-in [35]), which will be expanded upon later.

Shown in Figure 3.2 is the experimental setup including the drift tube, a 0.9 m length vacuum pipe connecting the target chamber to the detector chamber which allows for the initial spatial separation of the charged particles as the plasma expands towards the detector.

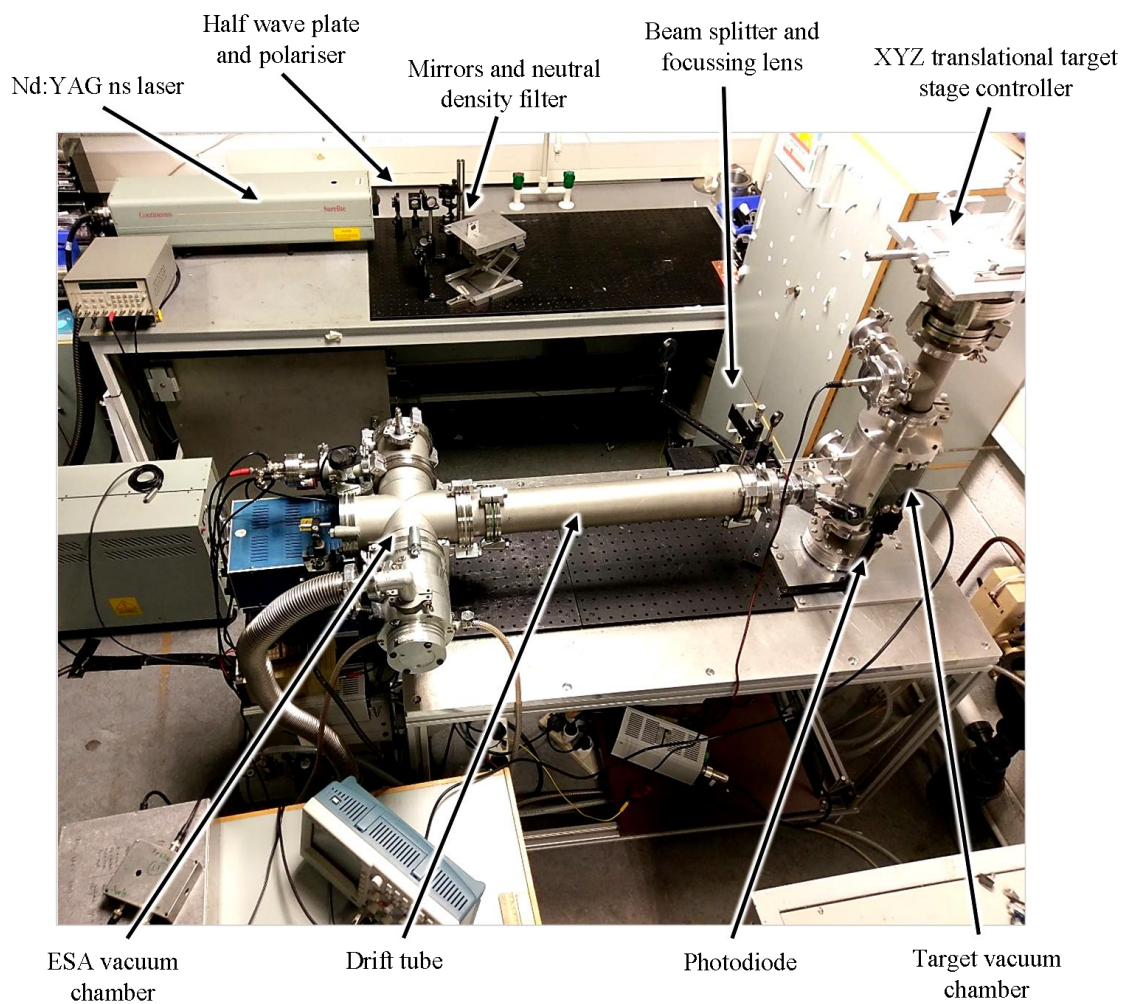


Figure 3-2: Photograph of the experimental setup showing the laser, optics, vacuum chambers and some electrical and vacuum equipment. The optics setup consists of a half wave plate, polarizer, mirrors, neutral density filter, and on the second table a beam splitting wedge and focussing lens.

The target comprised a machined block of non-oxygenated copper of rectangular shape into which grooves or wedges of angles 90° , 60° and 30° were cut.

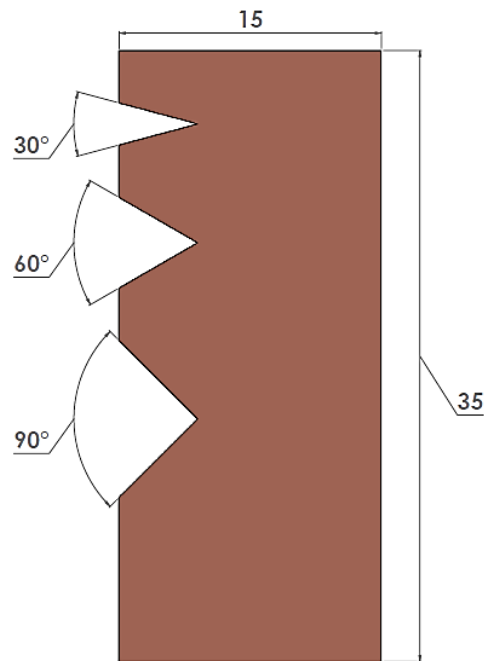


Figure 3-3: Diagram of the Cu target used, featuring the 90° , 60° and 30° wedges for colliding plasmas (units in mm).

The Cu used contained a small percentage ($\approx 2\%$) of carbon for ease of machining, as pure copper is quite difficult to reliably cut with high precision [36]. This is due to the high linear expansion coefficient, high plasticity, high heat conductivity and low hardness which all contribute to the copper tending to deform while it is being machined [37].

The ESA is housed within a vacuum chamber split into two parts: the first is used to house the target and XYZ translational stage and the second to contain the ESA itself. These two chambers are connected via CF flanges and the 0.9 m long pipe (with diameter 0.08 m) which acts as the drift tube for the system. This introduces the aforementioned charged particle discrimination into the experiment, as the distance travelled enables the charged particles in the expanding plasma to separate spatially. The expansion of the faster, lighter electrons creates an imbalance in the charge distribution, with a large negative bias at the plume front accelerating the positive charges via the ambipolar field created [38]. Particles with a higher positive charge undergo a greater acceleration so when the ion signal reaches the detector one first observes the highest charged states of the lighter ions based on the q/m ratio.

Connected to the drift tube is a vacuum valve that can be used to isolate the two chambers. Each chamber is fitted with a backing pump (or roughing pump), a turbo pump, a low-pressure gauge and a high-pressure gauge. To reduce the pressure in both chambers simultaneously Leybold Trivac D2-5E and D16B backing pumps were used, and for the turbomolecular pumps Turbovac 151 and 50 models respectively were used.

Using the dual-pump system over a period of 40 minutes the chambers can reach pressures of 10^{-6} mbar. This vacuum level is necessary to safely apply high voltages to the electron multiplier [35] within the ESA. If a large electrical bias is applied while the pressure is still high is likely to result in air breakdown causing a short-circuit across the channel electron multiplier (CEM), which could result in permanent damage to the detector. To avoid such a catastrophic occurrence the CEM is operated in vacuo and the applied voltage is ramped slowly from 0 – 1.8 kV. Higher voltages could be used to increase the detector gain, but this would also increase the noise, decreasing the m/q resolution and making isotope identification more difficult.

3.1 Nd:YAG Laser System

To generate the plasma a Q-switched Continuum Surelite III-10 laser system operating at 1064 nm was used. Pulses from this Nd:YAG laser possess a Gaussian spatial distribution and are linearly polarised. The system was operated from an external trigger in single shot mode throughout the experiment. The literature specifications for the system are as follows:

	Surelite III-10 Laser System
Wavelength (nm)	1064
Energy (mJ)	800
FWHM (ns)	6, 4 (harmonics)
Repetition Rate (Hz)	10 / single shot
External Trigger Jitter (ns)	≤ 1

Table 3.1: Surelite Continuum Nd:YAG laser specifications

Q-switching refers to the quality factor (Q-factor) of the resonator, and how this becomes degraded during operation to enable a higher gain. The Q-Switch itself is made up of a quarter-waveplate, a Pockels cell and a polariser within the oscillator. At peak population inversion the Q-factor is restored to its original higher value, allowing excited atoms to release their energy as photons in a high energy short pulse. This Surelite system operates in active Q-switching mode which necessitates an electro-optic gate within the resonator, enabling the controlled and rapid switching between high and low Q-factors. This results in high peak power, short duration laser pulses.

Within the oscillating cavity the beam makes a double-pass through the Pockels cell and the quarter-wave plate and undergoes a 90° rotation of linear polarisation, changing the originally horizontally polarised beam to vertical polarisation which is now rejected by the polarizer. If a high voltage is now applied to the Pockels cell it opens the cavity, causing a quarter-wave rotation of incoming photons. The original beam, having performed a double pass through the cavity, can now be transmitted as it is rotated a further 90° to be horizontally polarized again, passing through the polarizer and output coupler. This process and the population inversion occurs in a matter of ns, resulting in a pulse with a full width at half maximum (FWHM) of a few ns.

3.1.1 Optics Setup

At the exit of the laser there is an array of mirrors and optical devices for the purposes of redirecting, attenuating, focussing and splitting the laser beam. First there is an adjustable half-wave plate used to alter the polarisation state of the beam. Through rotation of the half wave plate one can continually adjust the polarisation direction of the beam which, in conjunction with the polariser placed just after it, allows one to achieve variable attenuation of the beam power to a large degree [39].

The half wave plate itself is made of a birefringent crystal cut parallel to the optical axis in the crystal face. When a light ray is incident to this surface the electrical field E is decomposed into two separate linearly polarised components (the component polarised parallel is known as the extraordinary beam, and the component polarised perpendicular

as the ordinary beam). When the ordinary beam has a higher index of refraction than the extraordinary beam then the polarisation directions along, and perpendicular, to the optical axis are known as the fast and slow axes. The phase difference between the two components of the beam after passing through the wave plate is some multiple of 180° or one $\frac{1}{2}$ wave.

One can achieve the full range of attenuation from the half wave plate by rotating it through 45° (e.g. 0° to 45°). The resulting intensity of the beam is then given by the expression:

$$I_1 = I_0 \cos^2(2\phi) \quad (3.1)$$

where I_1 represents the intensity of the transmitted beam, I_0 is the original intensity incident on the $1/2$ wave plate and ϕ is the azimuthal angle of the $\frac{1}{2}$ wave plate – by rotating the $\frac{1}{2}$ wave plate through an angle of ϕ one can achieve a 2ϕ degree rotation of polarisation of the beam. This beam of intensity I_1 then passes through the polarizer, using equation 3.1 again but reducing the previous 2ϕ factor to θ (the angle between the initial direction of polarization of the beam, and the axis of the polarizer), provided the waveplate and the polarise are aligned along the same axis.

The polarizer used comprised two calcite wedges pressed together with their optical axes parallel to one another. When the laser beam impinges upon the intersection, the electrical field is separated into its distinct S and P polarised components aligned with the fast and slow axes of the crystal. The cube has different indices of refraction for the S and P components, such that it is possible for the wedges to be angled so that the S polarized light will undergo total internal reflection while the P polarized light is able to pass with minimal disruption and is used for the eventual plasma plume generation. The reflected S component is absorbed by a beam-stop placed to one side of the polarizer.

In order to further decrease the beam fluence one can also place different neutral density filters in this optical system after the polarizer. This functions to reduce the intensity of any wavelength of light which passes through it as described below:

$$\text{Fractional transmittance} = \frac{I}{I_0} = 10^{-d}. \quad (3.2)$$

where I_0 is incident beam intensity, I is the transmitted intensity and d is the optical density of the filter. In this system a filter with an optical density ≈ 0.83 was used, which reduced the laser pulse energy from 493 to 73 mJ.

There is an array of dichroic mirrors, including a periscope, to redirect the beam such that it will impinge upon the metal target at the correct position and angle to be detected by the ESA. The beam splitter and focussing lens are located at the entrance to the vacuum chamber itself. The beam splitter consisted of a bi-prism which, when positioned correctly, will split the incoming beam evenly in half, outputting two identical beams with a well-defined angle between them. These beams then pass through a plano-convex lens and are focussed to a spot size of 0.5 mm diameter each separated by a 2 mm distance. The close proximity was necessary in order to ensure a stagnation layer would form at the collisional plane of the two plasmas, as at larger separation values the plasmas could be too diffuse upon collision. This small separation distance was also necessary in order to align the laser spots successfully along the walls of the narrower wedge shaped targets (this was important for the much narrower 30° wedge in particular, illustrated in Figure 3.3).

3.2 Energy Sector Analyser

The ESA (Energy Sector Analyser) is composed primarily of two narrow entrance and exit slits for the collimation of ion beams, a pair of curved electrically biased plates for the bending and kinetic energy separation of the ion beam and a final electron multiplier for amplification of the ion signal to be displayed on an oscilloscope.

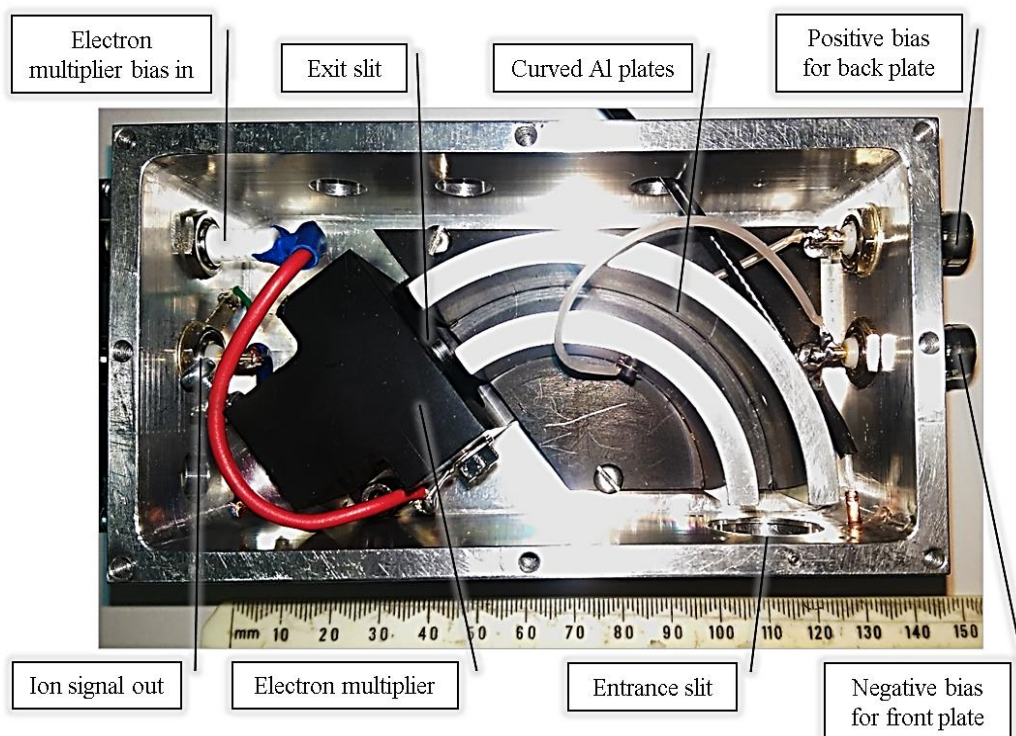


Figure 3-4: Photograph of the ESA detector showing the curved Al plates, exit/entrance slits and electron multiplier for signal amplification.

The collimating slits are placed at the entrance to the ESA and at the exit just in front of the electron multiplier. By altering the slit-widths one can decrease the amount of signal permitted to pass through to the detector. This helps to avoid signal saturation as well as collimating the ion beam. If they are too narrow then the signal will be extremely faint and hard to discern over the background noise. If they are too wide then the signal will be stronger, but the ion peaks will be broader and will exhibit poor resolution. Various dimensions were tested, and a slit width of 2 mm was decided upon, as a compromise between good signal strength and m/q resolution. The slit width however does not directly affect the m/q resolution. Rather, the mass resolution is determined by the time of flight, which is in turn dependent on E/q - thus the mass resolution is improved as a result of improving the energy resolution.

The two curved plates were machined from a solid aluminium block, chosen for its high electrical conductivity, machinability and durability. Applying opposite electrical biases to each plate creates a curved electrical field between their arcs. To examine the positively charged ions one can positively bias the back plate while the front plate is negatively biased. In order to detect negatively charged ions, the opposite biases can be applied to the curved plates and detector.

When a positively charged ion enters the electric field, with some kinetic energy, it is subject to an electrical force repelling it from the positively biased back plate [40]. The effect of this force as a function of the particle's kinetic energy is described by the following equation [41]:

$$q = \frac{1}{2} \frac{m d^2}{t^2 \Delta V} \left(\frac{r_1}{r_2} - \frac{r_2}{r_1} \right) \quad (3.3)$$

$$\Rightarrow E_p = \frac{q \Delta V}{\left(\frac{r_1}{r_2} - \frac{r_2}{r_1} \right)} \quad (3.4)$$

where q represents the ion charge, m is ion mass, d is distance from plasma formation to ESA, t is ion flight time, E_p stands for pass energy and is the kinetic energy that a particle must possess in order to pass through the inter-plate bias of magnitude ΔV , measured in volts and r_1 and r_2 represent the inner and outer radii of the curved plates which help to determine the distance of the path the ions will take through the ESA. This specific $r_1/r_2 - r_2/r_1$ factor comes from the radial field equation

$$\varepsilon(r) = \frac{\Delta V r_2 r_1}{(r_1 - r_2) r^2} \quad (3.5)$$

where r represents a particle's path between the curved plates, resulting in a circular orbit provided that $\varepsilon(r) = a m v_0^2 / q r^2$ where a is the acceleration experienced by the particle within the radial field, m is the particle mass, v_0 is the particle velocity prior to entering the radial fields and q is the charge on the particle. Hence, if $m v_0^2 = 2 q E$ (or rather, if E is the energy of the normal particle just prior to entering the radial field) and if $a = (r_2 + r_1) / 2$ then one arrives at the equation for the focussing potential of the detector, shown in equation 3.4 shown prior [40].

The plate bias ΔV is determined by the total net difference between the two oppositely biased plates, i.e. a 50 V bias is representative of -25 V applied to the front plate and +25 V applied to the back plate. In all cases ΔV implies that the front plate is at $-\Delta V / 2$ with respect to ground, and the back plate is at $+\Delta V / 2$ with respect to ground. Even if a particle possesses the correct energy, it does not simply "pass through" the electric field. Instead, due to the curvature of the plates, it will follow a path precisely along the centre radius of the plates, r_0 , and exit the electrical field still on the centre line – directly into the electron multiplier. A particle possessing higher or lower kinetic energy will not travel along this centre line and will instead either not be deflected enough from the original trajectory and will strike the back plate (kinetic energy too high) or undergo too

great a deflection by the electric field and strike the front plate (kinetic energy too low). Thus, one can alter the voltage applied to the plates to sweep through the range of kinetic energies of incoming particles, examining each kinetic energy ensemble set of ions individually and ultimately building up a picture of the entire kinetic energy spectrum of incoming ions [42].

Furthermore, building on the result from equation 3.3 one can extract a method for the calculation of the exact time of flight that an ion should have given a certain charge, mass, energy and plate voltage:

$$t = \sqrt{\frac{m \times d^2}{2 \times E_p}} \quad (3.6)$$

where t is the time of flight (generally on the scale of tens of microseconds), m is the mass of the ion to be examined (in kg) and d is the distance from the target to the detector (m) [43]. Using the previous two equations one can compile the following tables of Cu, C and H time-of-flight (ToF) values.

Cu	Volts	50		75		100		150		200			
		q	Isotope	^{63}Cu	^{65}Cu	^{63}Cu	^{65}Cu	^{63}Cu	^{65}Cu	C^{63}	^{65}Cu	^{63}Cu	^{65}Cu
1	t (μs)			50.84	51.66	41.51	42.17	35.95	36.52	29.35	29.82	25.42	25.82
2	t (μs)			35.95	36.53	29.35	29.82	25.42	25.82	20.75	21.08	17.97	18.26
3	t (μs)			29.35	29.82	23.97	24.34	20.75	21.08	16.95	17.21	14.68	14.91
4	t (μs)			25.42	25.83	20.75	21.08	17.97	18.26	14.68	14.91	12.71	12.91
5	t (μs)			22.74	23.10	18.56	18.86	16.08	16.33	13.13	13.33	11.37	11.55

Table 3.2: Calculated Cu isotope ToF values at various plate biases for the first five ionisation stages

C	Volts	50		75		100		150		200		
		q	Isotope	^{12}C								
1	t (μs)			22.21	18.14	15.71	12.82	11.11	9.07	7.85	6.41	5.55
2	t (μs)			15.71	12.82	11.11	9.07	7.85	6.41	5.55	4.97	4.97
3	t (μs)			12.82	10.47	9.07	7.40	6.41	5.55	4.97	4.97	4.97
4	t (μs)			11.11	9.07	7.85	6.41	5.55	4.97	4.97	4.97	4.97
5	t (μs)			9.93	8.11	7.02	5.73	4.97	4.97	4.97	4.97	4.97

Table 3.3: Calculated C isotope ToF values at various plate biases for the first five ionisation stages

H	Volts	50	75	100	150	200
---	-------	----	----	-----	-----	-----

q	Isotope	^1H	^1H	^1H	^1H	^1H
1	t (μs)	6.434	5.254	4.550	3.715	3.217

Table 3.4: Calculated H isotope ToF values at various plate biases

These calculated values allow one to state with some certainty exactly which elements and charge states are observed based on their ToF values.

The current dimensions of the detector used here are as follows:

Component	Dimensions
Curved plate outer radius (r_1)	0.039 m
Curved plate inner radius (r_2)	0.031 m
Curved plate separation distance	0.008 m
Angle subtended by curved plates (φ)	127°
Curved plate arc length (R)	0.078 m
Target to detector distance	0.925 m
Slits widths (Ω)	0.002 m
Distance from ESA entrance to electron multiplier along r_0	0.100 m
Distance from sector field (curved plate) exit to centre of exit aperture (δ)	0.008 m

Table 3.5: ESA-ToF mass spectrometer dimensions

The entire device is electrically isolated in a grounded aluminium box of dimensions $0.15 \times 0.075 \times 0.05 \text{ m}^3$.

By combining equations 3.3 and 3.4 one can calculate the detector energy resolution as follows:

$$\frac{\Delta E}{E} = \frac{\Omega}{(R(1 - \cos(\varphi)) + \delta \sin(\varphi))} \quad (3.7)$$

ΔE represents the full width at half maximum (FWHM) of an energy signal, φ is the radial angle of the curved plates, δ is the distance between the exit of the curved plates sector field and the centre of the exit aperture (electron multiplier), R is the centre radius path between the curved plates and Ω is the slit width used. Taking the dimensions from Table 2 one can calculate the resolution value:

$$\frac{\Delta E}{E} = \frac{0.002}{(0.035(1 - \cos(127)) + 0.008 \times \sin(127))} \quad (3.8)$$

For the ESA dimensions used one calculates a value of $\Delta E/E = 0.032$ or $\approx 3\%$ of the pass energy – it should be noted that this is the uncertainty value is due to the ESA physical dimensions alone. Also, it is the uncertainty that one observes for a single shot. However for each voltage and target type a total of 25 shots were recorded, which were then averaged to limit the background noise and interference in the signal. The table below serves to compare the theoretical and experimental values for the ToF signals.

One must also take into account the errors due to device fabrication imperfections, random particle collisions as the plasma expands along the drift tube length and electrical noise generated from the circuit systems used. Comparing the experimental to the calculated ToF values one can obtain the following values, in this case for the ion signal received from a single laser pulse on a flat Cu target at a plate bias of 100 V.

Cu		$^{63}\text{Cu}^{1+}$	$^{65}\text{Cu}^{1+}$	$^{63}\text{Cu}^{2+}$	$^{65}\text{Cu}^{2+}$	$^{63}\text{Cu}^{3+}$	$^{65}\text{Cu}^{3+}$	$^{63}\text{Cu}^{4+}$	$^{65}\text{Cu}^{4+}$
Theoretical		36.0	36.5	25.4	25.8	20.8	21.1	18.0	18.3
Experimental		35.8	36.4	25.3	25.9	20.6	21.1	17.8	18.1
Deviation (μs)		0.2	0.1	0.1	0.1	0.2	0.0	0.2	0.2
C		$^{12}\text{C}^{1+}$	$^{12}\text{C}^{2+}$						
Theoretical		15.7	11.1						
Experimental		15.7	11.1						
Deviation (μs)		0.0	0.0						
H		$^1\text{H}^{1+}$							
Theoretical		4.6							
Experimental		4.7							
Deviation (μs)		0.1							
Summary		Average							
Deviation (μs)		0.1							

Table 3.6: Tabulated values of the calculated vs experimental ToF (μs) for isotopes from a flat target at a plate bias of 100 V, showing the average discrepancy in the ToF signal is $\sim 0.1 - 0.2 \mu\text{s}$.

E_p (eV)	$\Delta V = 50$ V	75 V	100 V	150 V	200 V
$q = 1$	108	162	216	324	432
2	216	324	432	648	864
3	324	486	648	972	1295
4	432	648	864	1295	1727
5	540	810	1080	1619	2159

Table 3.7: List of the pass energies of ions in eV at the ΔV values used.

To record various kinetic energies of charge states a range of plate biases was used, increasing from the lowest bias and well-resolved signal to the highest bias, where the signal started to fade away completely. This resulted in an operating plate bias range of 50-200 V where the vast majority of the ions appeared. The actual values selected were 50V, 75V, 100V, 150V and 200 V. This translates to the following kinetic energies from the lowest charge state for the lowest plate bias used, to the maximum charge state observable for the highest plate bias used.

For each plate bias ΔV the various charge states q of Cu, C and H can have the same pass energy but will arrive at the detector at different times owing to their different m/q ratios leading to their spatial separation. Hence one can determine which ion stages are most abundant at different kinetic energies for the range of target geometries used. These ToF and kinetic energy values for the plasma are in accordance with the values typically observed in laser produced colliding plasmas [12], [44].

3.2.1 Alignment

When initially setting up the systems it was necessary to devise a method to correctly align the ESA entrance slit with the laser spot upon the target. With a 2 mm aperture entrance on the ESA and a 0.925 m distance from ESA to target, there was a very limited range of suitable angles for the ESA. If the alignment was even a few degrees off one could not detect any ion signal from the ESA.

To align the ESA with the plasma a small adjustable laser pointer was set up behind the ESA chamber and aligned with a series of holes bored in the ESA walls and curved plates to strike the centre of the Cu target. This spot was used as a guide to line up the Nd:YAG laser at the same spot so that when the chambers were evacuated the laser-produced plasma could expand in a direction perpendicular to the target directly towards the detector. This delicate alignment process took some time to execute using very minute adjustments which were achieved by having a setup that allowed multiple degrees of fine tuning. The laser pointer, ESA and target were all attached to multi-axis translation stages allowing one to fine-tune the angular and x-y-z positions of the detector. One could also remove these components from the alignment stages to facilitate experimental setup and replace them accurately during data gathering.

4 Results and Analysis

4.1 Initial Observations

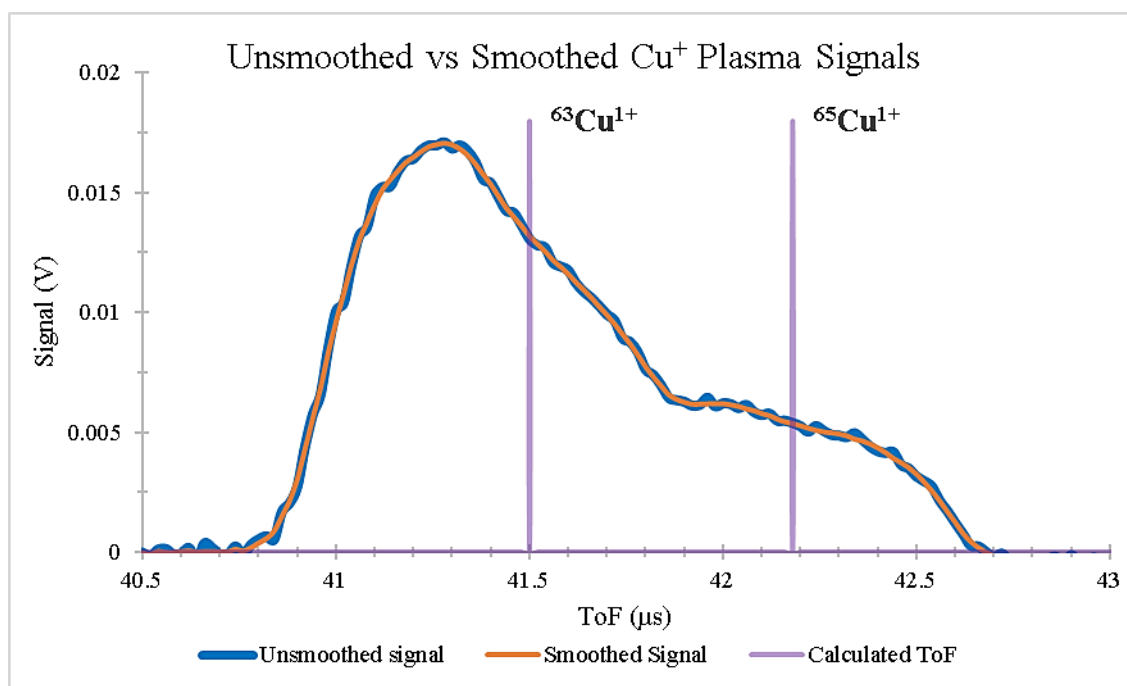


Figure 4-1: Comparison of the initial and smoothed ESA signals following application of the Savitzky-Golay filter. This signal shows the 1st charged state of Cu⁺ from a colliding plasma on a flat Cu target at a plate bias of 75 V.

Before the ion signals recorded from different targets could be compared it was important to first improve the resolution of the ESA signal and remove some of the background noise using a digital smoothing filter (Figure 4.1). To this end a Savitzky-Golay function was fitted over the signals taken, using the method of least squares

smoothing to fit a second-degree polynomial over each 10-point window of data points [45].

The following figures 4.2 and 4.3 show some sample plots with a 75V plate bias, structurally typical of most of the plasma signals observed. Figure 4.2 shows ToF signals for the three plume types (single plume-full laser pulse energy, single plume-half pulse energy and a pair of colliding plasmas) formed on a flat target while Figure 4.3 shows the ion signals from the three wedge shaped targets on which colliding plasmas were formed. Superimposed on these figures are the calculated ToF data for the Cu, C and H isotopes from Tables 3.2, 3.3 and 3.4. The fitted isotope ToF values provide information on which charge states and isotopes are present in the plasma plumes, and how the charge state distribution varies with kinetic energy, laser fluence and target geometry. The normal isotope distribution for Cu is $\frac{3}{4}$ ^{63}Cu and $\frac{1}{4}$ ^{65}Cu which is reflected in the isotope peak ratios.

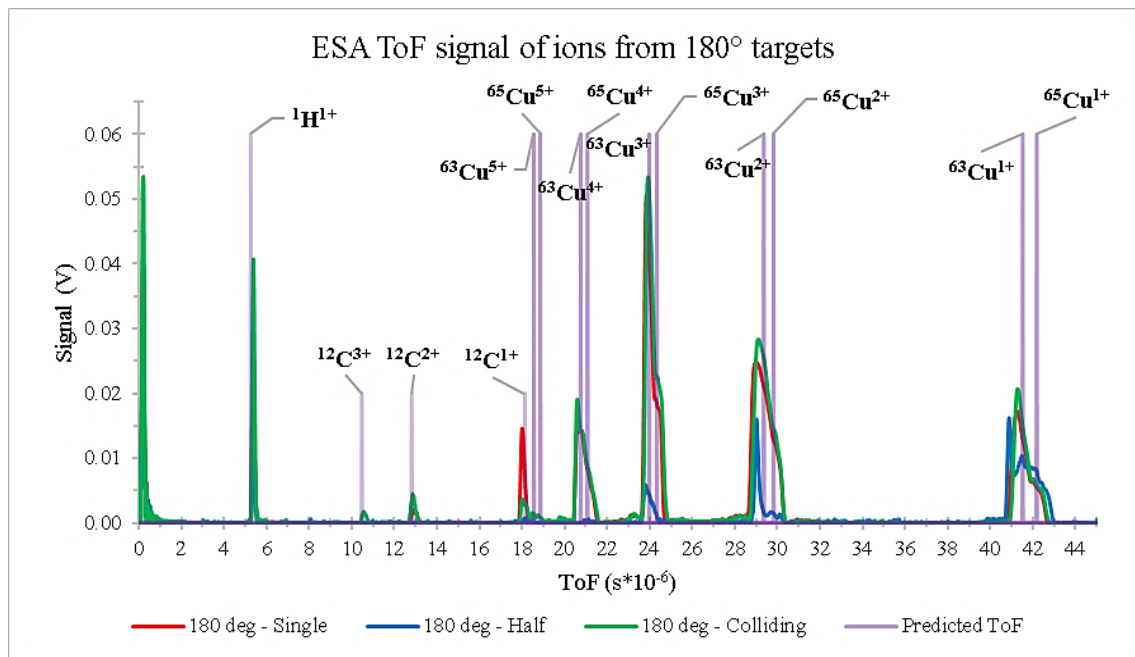


Figure 4-2: Ion ToF signals for a single laser pulse, half a pulse and two colliding plasmas on a flat target.

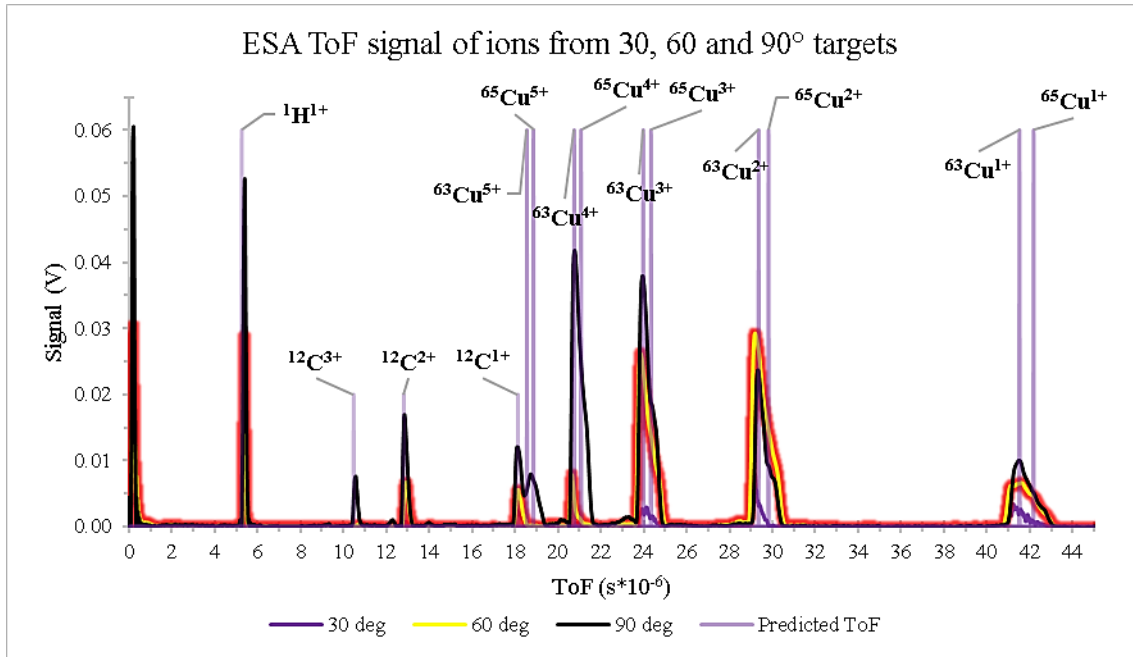


Figure 4-3: Ion ToF signals from colliding plasmas formed on 30°, 60° and 90° wedge targets.

In the lowly charged ion signals a number of small extra peaks are present which do not correspond to the expected double isotope shape for Cu ions. These extra peaks are brought about by a combination of the random noise present in each signal and the averaging of 25 different signals to form the data presented. Slight shifts in the ion ToF values over 25 separate signals results in the presence of the smaller peaks. These are most apparent for the more lowly charged states due to the larger separations in the ToF values and hence broader peaks but are less noticeable for the more highly charged states.

It is possible to obtain signals with a higher resolution, as shown in Figure 4.4, but the conditions necessary for this pose further difficulties which are discussed later. Figures 4.4 and 4.5 show the ion signals from a single plasma plume on a flat target and that of a colliding plasma from a 60° wedge target, for a plate bias of 75 V, a total laser fluence of 73 mJ and an electron multiplier voltage of 1.668 kV.

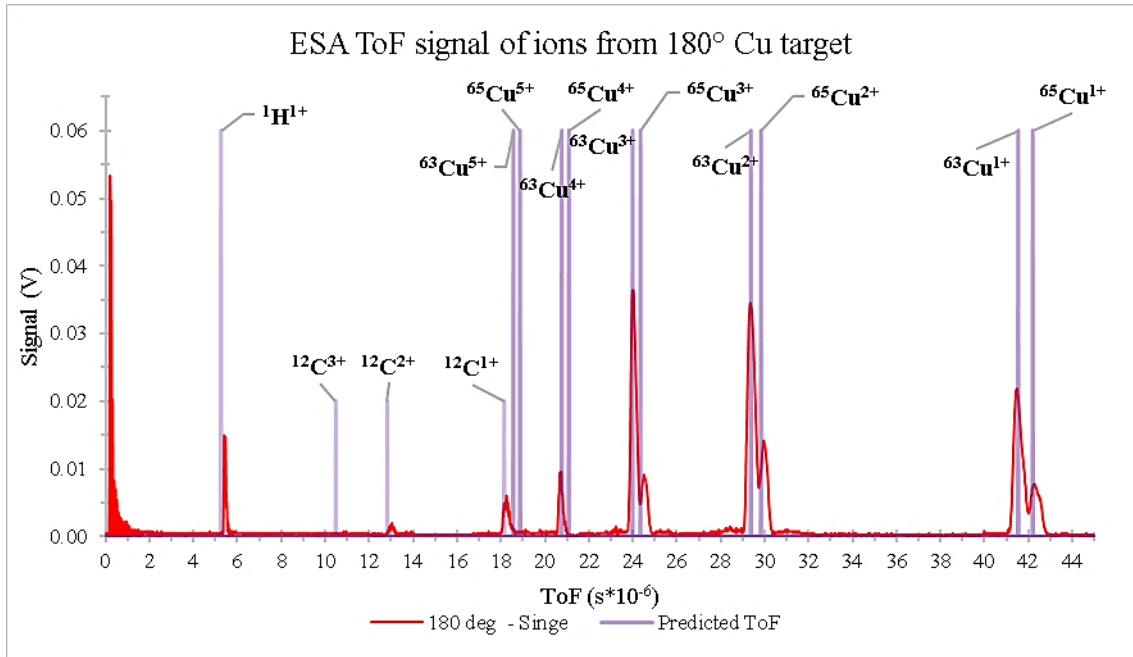


Figure 4-4: Ion ToF signal of a single 73 mJ laser pulse on a 180° Cu target at a 75 V plate bias with CEM voltage of 1.668 kV

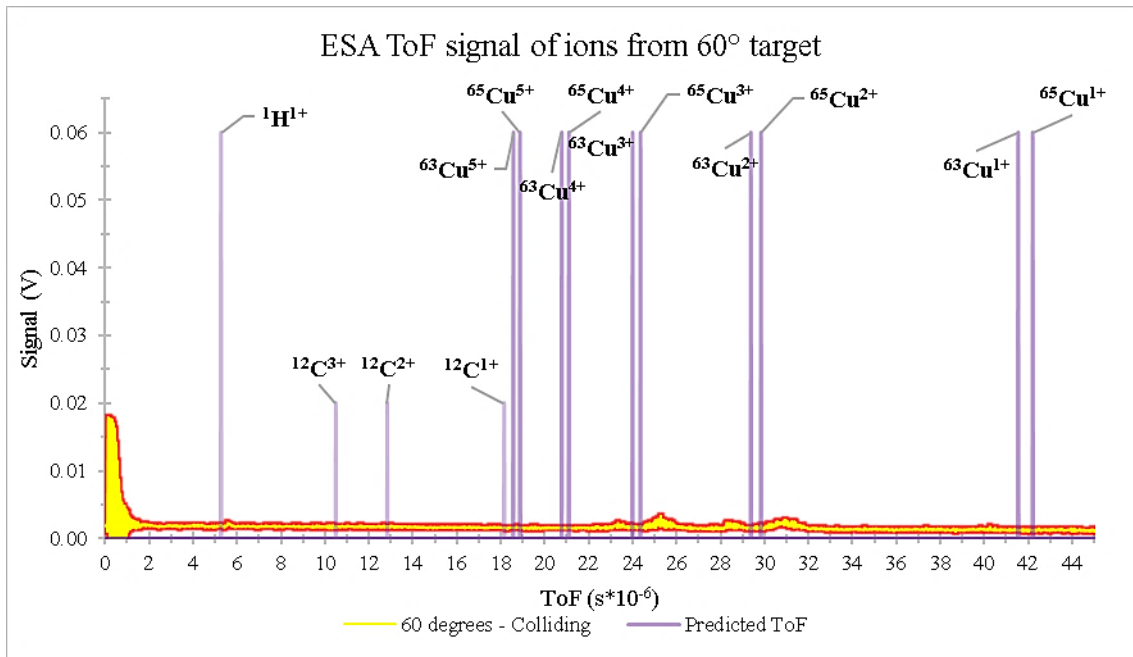


Figure 4-5: Ion ToF signal of a single 73 mJ laser pulse on a 60° Cu target at a 75 V plate bias with CEM voltage of 1.668 kV

As can be seen from Figures 4.4 and 4.5 two ToF traces can be quite different. Hence optimisation of the CEM bias is needed for each experiment in order to obtain very highly resolved isotope peaks.

In order to achieve narrow and hence well-defined isotope peaks the voltage applied to the electron multiplier must be altered to match the required values for each target, plasma type and pass energy used. In order to see the 60° signal a higher voltage on the CEM is needed, but this decreases the definition for other signals. In practice one must employ a voltage of between 1.5 and 2.8 kV to obtain a high-resolution ToF trace for all targets used and their associated plasma conditions.

Using such a wide range of voltages makes direct comparisons difficult, as each signal is amplified to a different degree. While this did yield clear (high resolution) ToF traces such as Figure 4.4, it was decided to settle on a mid-range voltage of 1.8 kV, using the same values for each signal recorded during the experiment- keeping a fixed, stable voltage whilst still maintaining a satisfactory resolution. Given more time it would have been preferable to record signals at the optimum voltage to obtain maximum resolution for each data set and normalize all such sets to allow for direct comparisons without the unequal amplification factor.

In order to accurately measure the integrated signal under each isotope peak one can fit a Gaussian shaped function to each peak using Fityk software [46]. This becomes very useful when the raw ToF resolution is not sufficient. The program can be used to easily fit numerous peaks of various functions to one TOF trace, meaning from a poorly resolved Cu peak one can accurately fit the form of the expected isotope peaks that would otherwise have been more visible at greater m/q resolution. This method provides values for the area, signal height and ToF for each isotope peak. Using the pass energy calculations (equation 3.3) one can determine the exact ToF for different charge states and/or isotopes. Thus for a broad poorly defined peak at 25 μs , after calculating where the two distinct isotopes should be observed for Cu^{2+} one can fit two separate Gaussian shaped curves to this broad peak. Figure 4.6 shows this method using the signal from a colliding plasma on a flat Cu target with a 100 V plate bias.

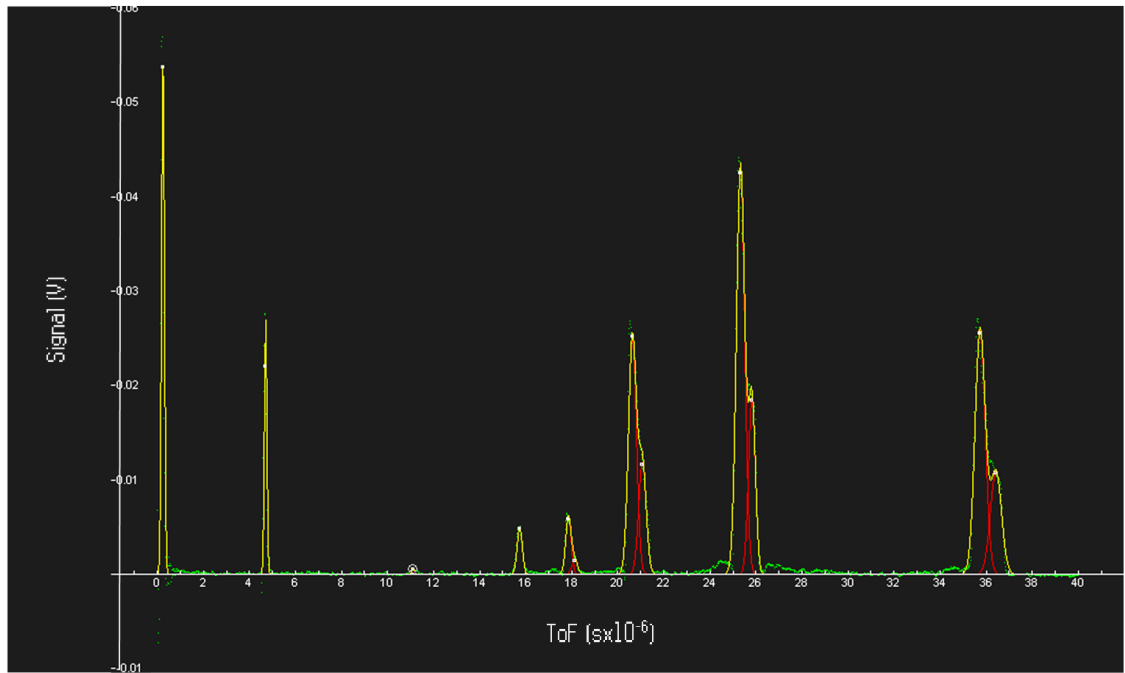


Figure 4-6: Ion ToF signal from a 100 V biased ESA with fitted peaks to highlight the presence of ^{63}Cu , ^{65}Cu , ^{12}C and ^1H isotopes for each charged state as well as an initial laser photopeak.

By fitting such profiles to each discrete feature in the overall ToF signal one can obtain a more accurate view of how the ion distribution evolves with decreasing target wedge angle. These fitted peaks also reflect the expected natural isotopic abundance ratio of $\approx 70:30$ for ^{63}Cu and ^{65}Cu respectively.

4.2 Ion Signal Presentation and Analysis

The graphs and tables below serve to better illustrate the changing ion stage distributions by displaying only the area under each ion/isotope peak for the different target types and pass energies. To obtain these values the area under each isotope peak from the ESA signals was integrated separately, and the resulting values were then plotted in terms of their atomic mass (Cu, C, H) and charge state (+1, +2, +3 etc). With a large number of data sets to consider it was decided to display the ion signals from flat targets and the signals from wedge shaped targets separately, as seen below in Figures 4.7 – 4.16.

For these figures 180° – S represents a single unsplit laser pulse impinging upon the flat Cu target, 180° – H represents half of this (a single seed plume) and 180° – C corresponds to two seed plumes from the split initial pulse creating the colliding plasmas used to bring about stagnation. 90°, 60° and 30° refer to the various target wedge angles used.

The errors displayed in the top right corner of each graph were calculated from the raw data obtained directly by the ESA before any averaging or noise filtering was carried out. For each target configuration (30°, 60°, 90°, 180°- C, H, S) and each plate bias (50, 75, 100, 150, 200 V) a total of 25 shots were recorded. By measuring the standard deviation of the area under each ion peak ($^{63}\text{Cu}^{+1}$, $^{65}\text{Cu}^{+1}$, $^{63}\text{Cu}^{+2}$, $^{65}\text{Cu}^{+2}$ etc) across those 25 samples, the average standard deviation (σ) could be calculated using the following formula.

$$\text{Standard Deviation} = \sigma = \sqrt{\frac{\sum(x - \bar{x})^2}{n}} \quad (4.1)$$

Here x becomes each value (area under ion peak) within the sample set, \bar{x} is the mean value of the set and n is the total number of values. This was calculated for each ion peak separately and then averaged, resulting in the values of 7% for Cu and 12% for C. The larger error value for carbon ions is attributed to the smaller peak size and the resultant increased difficulty in defining these smaller ion peaks against the background noise of the signal.

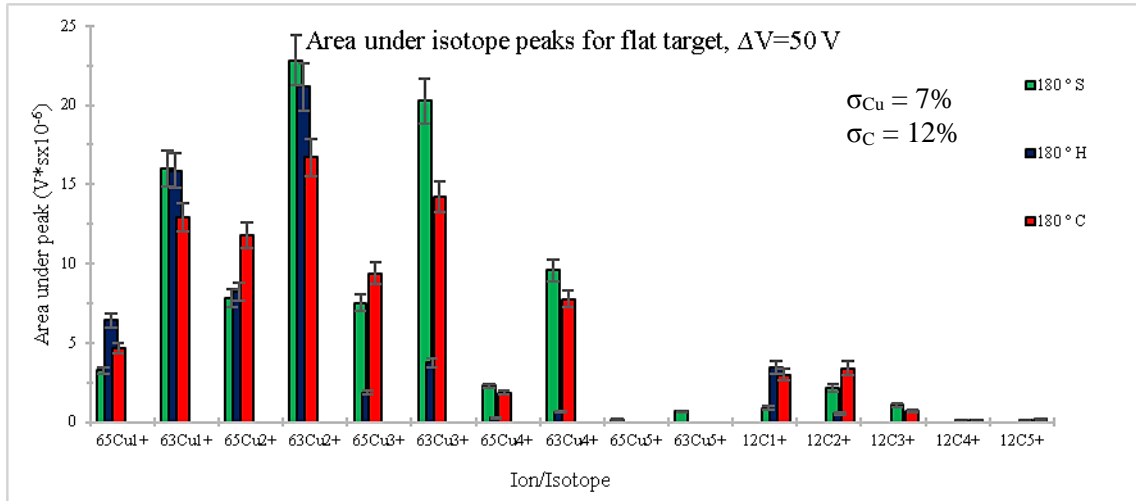


Figure 4-7: Histogram of isotope signals at a plate bias of 50 V for a flat target for a single laser pulse, half the original laser pulse energy, and the original beam split in two for a colliding plasma

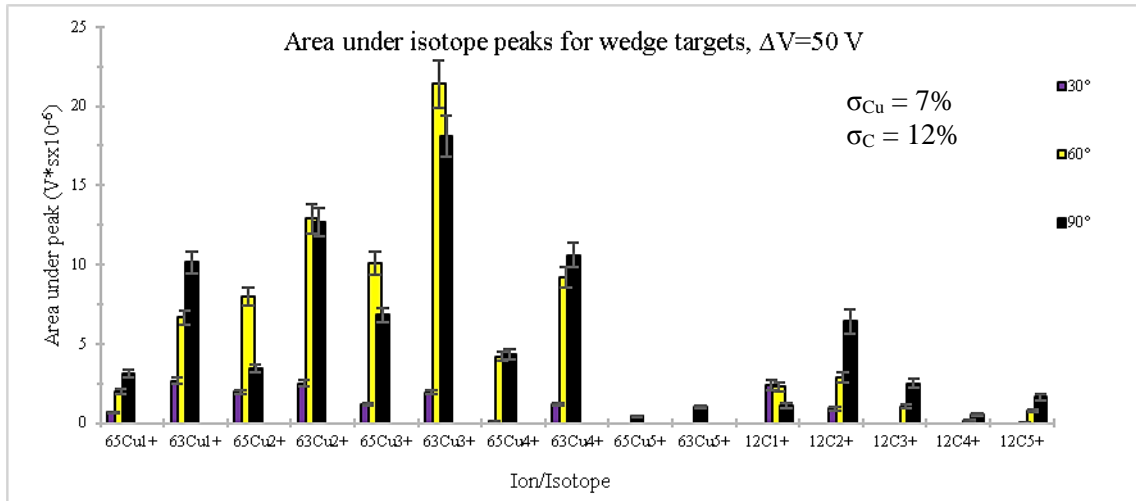


Figure 4-8: Histogram of isotope signals at a plate bias of 50 V for 3 different wedge targets – 90°, 60° and 30°

$\Delta V = 50$	180° - S	180° - H	180° - C	30°	60°	90°	Max (1)	Max (2)	Max (3)
$^{65}\text{Cu}^{1+}$	3.2	6.4	4.6	0.7	2.0	3.1	180° - H	180° - C	180° - S
$^{63}\text{Cu}^{1+}$	16.0	15.9	12.9	2.7	6.7	10.1	180° - S	180° - H	180° - C
$^{65}\text{Cu}^{2+}$	7.8	8.2	11.8	2.0	8.0	3.4	180° - C	180° - H	60°
$^{63}\text{Cu}^{2+}$	22.8	21.1	16.7	2.5	12.9	12.7	180° - S	180° - H	180° - C
$^{65}\text{Cu}^{3+}$	7.5	1.8	9.4	1.2	10.1	6.8	60°	180° - C	180° - S
$^{63}\text{Cu}^{3+}$	20.3	3.7	14.2	1.9	21.4	18.1	60°	180° - S	90°
$^{65}\text{Cu}^{4+}$	2.3	0.3	1.8	0.1	4.2	4.3	90°	60°	180° - S
$^{63}\text{Cu}^{4+}$	9.6	0.6	7.8	1.2	9.2	10.6	90°	180° - S	60°
$^{65}\text{Cu}^{5+}$	0.2	-	-	-	-	0.4	90°	180° - S	-
$^{63}\text{Cu}^{5+}$	0.7	-	-	-	-	1.0	90°	180° - S	-
$^{12}\text{C}^{1+}$	0.9	3.5	3.0	2.4	2.3	1.1	180° - H	180° - C	30°
$^{12}\text{C}^{2+}$	2.2	0.5	3.4	0.9	2.9	6.4	90°	180° - C	60°
$^{12}\text{C}^{3+}$	1.1	-	0.7	-	1.0	2.5	90°	180° - S	60°
$^{12}\text{C}^{4+}$	0.1	-	0.1	-	0.2	0.5	90°	60°	180° - C
$^{12}\text{C}^{5+}$	0.1	-	0.2	0.1	0.8	1.6	90°	60°	180° - C
$^1\text{H}^{1+}$	7.8	3.4	7.2	3.1	6.3	12.1	90°	180° - S	180° - C
Total	102.4	65.6	93.8	18.6	87.8	94.9	180° - S	90°	180° - C

Table 4.1: Tabulated values of the area under each isotope peak ($\text{V} \cdot \text{s} \cdot 10^{-6}$) at a 50 V plate bias

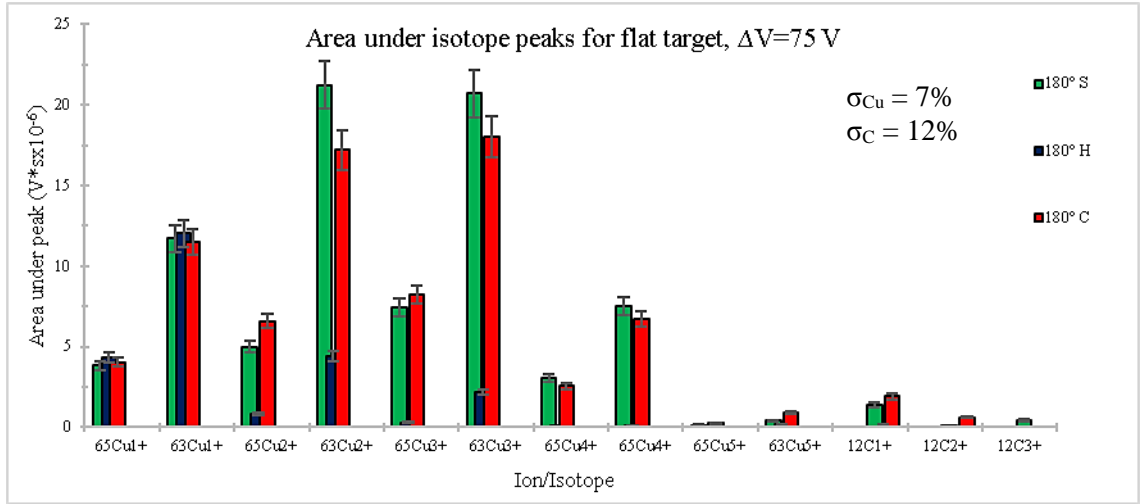


Figure 4-9: Histogram of isotope signals at a plate bias of 75 V for a flat target for a single laser pulse, half the original laser pulse energy, and the original beam split in two for a colliding plasma

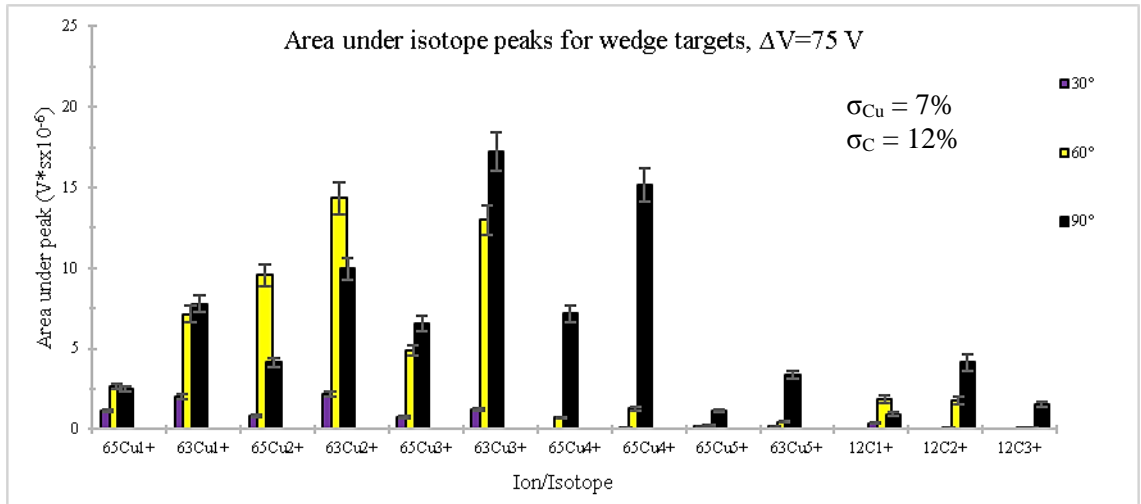


Figure 4-10: Histogram of isotope signals at a plate bias of 75 V for 3 different wedge targets – 90°, 60° and 30°

$\Delta V = 75$	180° - S	180° - H	180° - C	30°	60°	90°	Max (1)	Max (2)	Max (3)
$^{65}\text{Cu}^{1+}$	3.8	4.4	4.0	1.2	2.7	2.5	180° - H	180° - C	180° - S
$^{63}\text{Cu}^{1+}$	11.7	12.0	11.5	2.0	7.2	7.8	180° - S	180° - C	180° - H
$^{65}\text{Cu}^{2+}$	5.0	0.9	6.6	0.8	9.6	4.2	60°	180° - C	180° - S
$^{63}\text{Cu}^{2+}$	21.2	4.4	17.2	2.2	14.3	10.0	180° - S	180° - C	60°
$^{65}\text{Cu}^{3+}$	7.4	0.3	8.2	0.8	4.9	6.6	180° - C	180° - S	90°
$^{63}\text{Cu}^{3+}$	20.7	2.2	18.0	1.2	13.0	17.2	180° - S	180° - C	90°
$^{65}\text{Cu}^{4+}$	3.1	0.1	2.6	-	0.7	7.2	90°	180° - S	180° - C
$^{65}\text{Cu}^{4+}$	7.5	0.1	6.8	0.1	1.3	15.2	90°	180° - S	180° - C
$^{65}\text{Cu}^{5+}$	0.2	0.1	0.3	0.2	0.3	1.1	90°	180° - C	60°
$^{63}\text{Cu}^{5+}$	0.4	0.2	0.9	0.2	0.5	3.4	90°	180° - C	60°
$^{12}\text{C}^{1+}$	1.4	0.2	1.9	0.4	1.9	1.0	180° - C	60°	180° - S
$^{12}\text{C}^{2+}$	0.1	-	0.6	0.1	1.8	4.1	90°	60°	180° - C
$^{12}\text{C}^{3+}$	0.4	-	-	0.1	0.1	1.6	90°	180° - S	60°/30°
$^1\text{H}^{1+}$	5.6	1.7	3.6	1.5	3.8	7.5	90°	180° - S	60°
Total	88.6	26.4	82.2	10.8	61.9	89.2	90°	180° - S	180° - C

Table 4.2: Tabulated values of the area under each isotope peak ($\text{V} \cdot \text{s} \cdot 10^{-6}$) at a 75 V plate bias

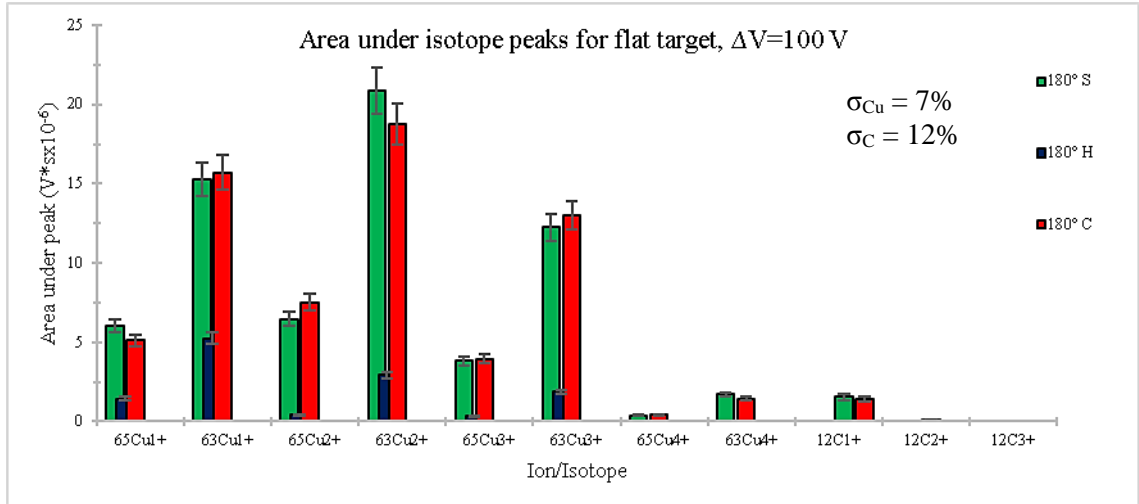


Figure 4-11: Histogram of isotope signals at a plate bias of 100 V for a flat target for a single laser pulse, half the original laser pulse energy, and the original beam split in two for a colliding plasma

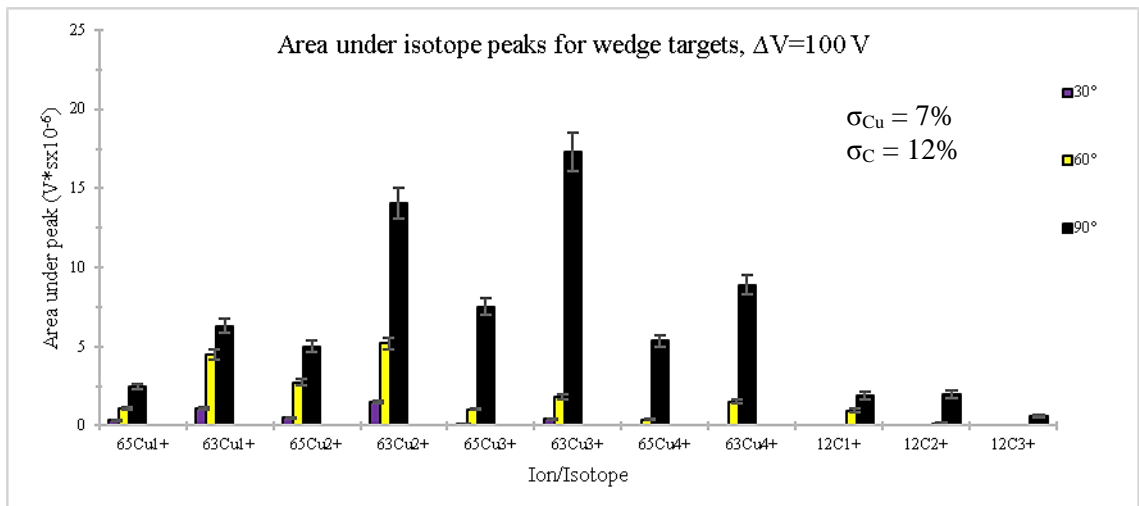


Figure 4-12: Histogram of isotope signals at a plate bias of 100 V for 3 different wedge targets – 90°, 60° and 30°

$\Delta V = 100$	180° - S	180° - H	180° - C	30°	60°	90°	Max (1)	Max (2)	Max (3)
$^{65}\text{Cu}^{1+}$	6.1	1.4	5.1	0.3	1.1	2.5	180° - S	180° - C	90°
$^{63}\text{Cu}^{1+}$	15.3	5.3	15.7	1.1	4.5	6.3	180° - C	180° - S	90°
$^{65}\text{Cu}^{2+}$	6.5	0.5	7.5	0.5	2.7	5.0	180° - C	180° - S	90°
$^{63}\text{Cu}^{2+}$	20.8	2.9	18.8	1.5	5.2	14.1	180° - S	180° - C	90°
$^{65}\text{Cu}^{3+}$	3.8	0.3	4.0	0.1	1.1	7.5	90°	180° - C	180° - S
$^{63}\text{Cu}^{3+}$	12.2	1.9	13.0	0.4	1.8	17.3	90°	180° - C	180° - S
$^{65}\text{Cu}^{4+}$	0.4	-	0.4	-	0.4	5.4	90°	180° - C	60°
$^{63}\text{Cu}^{4+}$	1.7	-	1.4	-	1.5	8.9	90°	180° - S	60°
$^{12}\text{C}^{1+}$	1.5	-	1.4	0.1	0.9	1.9	90°	180° - S	60°
$^{12}\text{C}^{2+}$	0.1	-	-	-	0.2	2.0	90°	60°	180° - S
$^{12}\text{C}^{3+}$	-	-	-	-	-	0.6	90°	-	-
$^1\text{H}^{1+}$	3.7	0.3	2.3	0.8	2.5	4.1	90°	180° - S	60°
Total	72.1	12.6	69.6	4.9	21.9	75.5	90°	180° - S	180° - C

Table 4.3: Tabulated values of the area under each isotope peak ($\text{V}\cdot\text{s}\cdot 10^{-6}$) at a 100 V plate bias

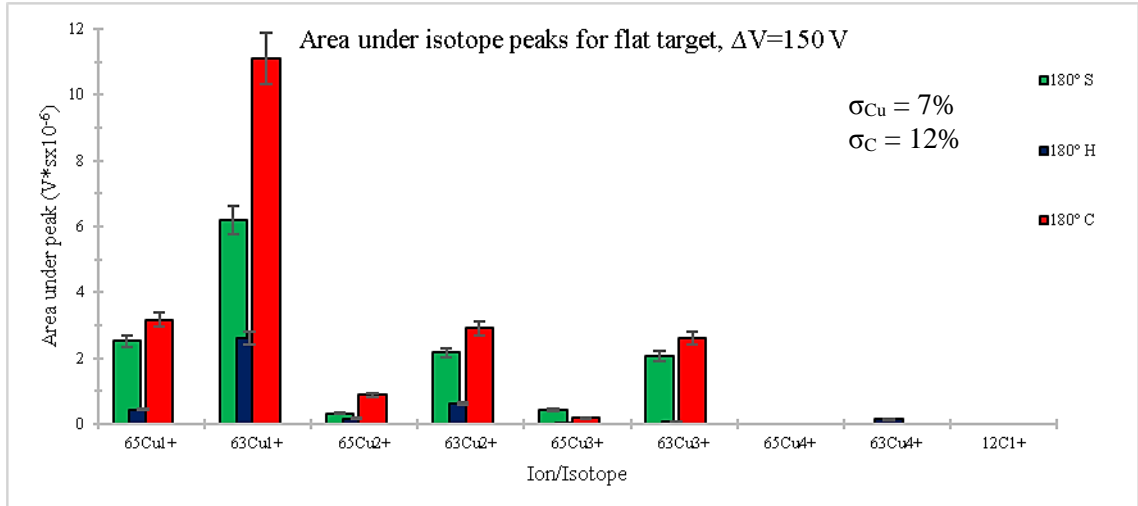


Figure 4-13: Histogram of isotope signals at a plate bias of 150 V for a flat target for a single laser pulse, half the original laser pulse energy, and the original beam split in two for a colliding plasma

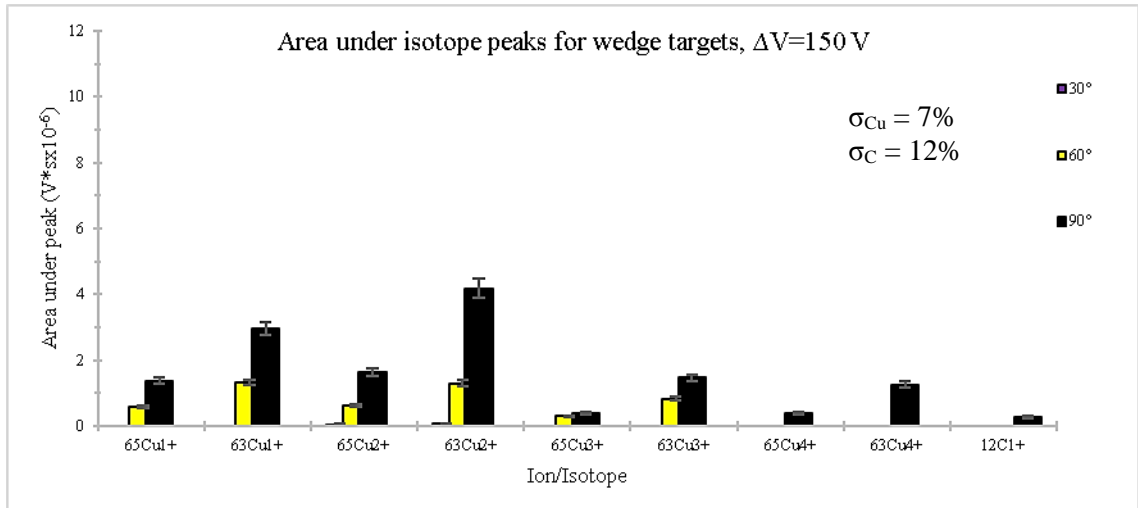


Figure 4-14: Histogram of isotope signals at a plate bias of 150 V for 3 different wedge targets – 90°, 60° and 30°

$\Delta V = 150$	180° - S	180° - H	180° - C	30°	60°	90°	Max (1)	Max (2)	Max (3)
$^{65}\text{Cu}^{1+}$	2.5	0.5	3.2	-	0.6	1.4	180° - C	180° - S	90°
$^{63}\text{Cu}^{1+}$	6.2	2.6	11.1	-	1.3	3.0	180° - C	180° - S	90°
$^{65}\text{Cu}^{2+}$	0.3	0.2	0.9	0.1	0.6	1.6	90°	180° - C	60°
$^{63}\text{Cu}^{2+}$	2.2	0.6	2.9	0.1	1.3	4.2	90°	180° - C	180° - S
$^{65}\text{Cu}^{3+}$	0.4	0.0	0.2	-	0.3	0.4	180° - S	90°	60°
$^{63}\text{Cu}^{3+}$	2.1	0.1	2.6	-	0.8	1.5	180° - C	180° - S	90°
$^{65}\text{Cu}^{4+}$	-	-	-	-	-	0.4	90°	-	-
$^{63}\text{Cu}^{4+}$	-	0.2	-	-	-	1.3	90°	180° - H	-
$^{12}\text{C}^{1+}$	-	-	-	-	-	0.3	90°	60°	180° - S
$^1\text{H}^{1+}$	0.2	-	0.1	-	0.1	0.6	90°	180° - S	180° - C
Total	13.9	4.2	21.0	0.2	5.2	14.6	180° - C	90°	180° - S

Table 4.4: Tabulated values of the area under each isotope peak ($\text{V} \cdot \text{s} \cdot 10^{-6}$) at a 150 V plate bias

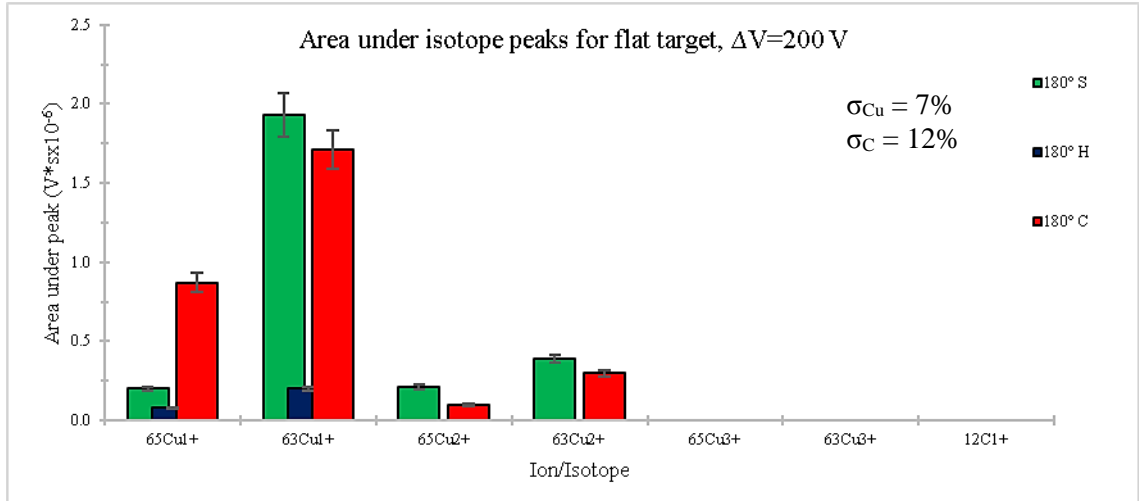


Figure 4-15: Histogram of isotope signals at a plate bias of 200 V for a flat target for a single laser pulse, half the original laser pulse energy, and the original beam split in two for a colliding plasma

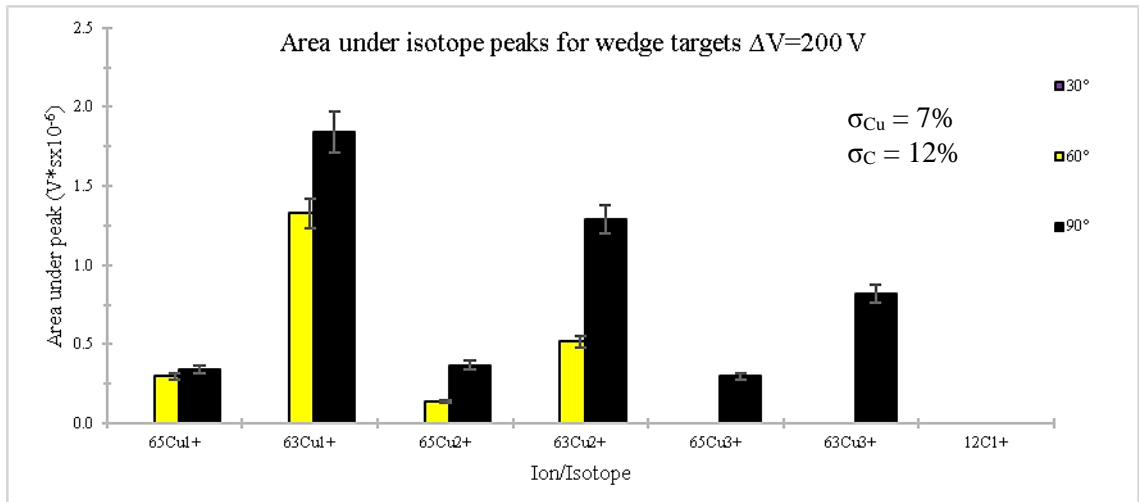


Figure 4-16: Histogram of isotope signals at a plate bias of 200 V for 3 different wedge targets – 90°, 60° and 30°

$\Delta V = 200$	180° - S	180° - H	180° - C	30°	60°	90°	Max (1)	Max (2)	Max (3)
$^{65}\text{Cu}^{1+}$	0.2	0.1	0.9	-	0.3	0.3	180° - C	90°	60°
$^{63}\text{Cu}^{1+}$	1.9	0.2	1.7	-	1.3	1.8	180° - S	90°	180° - C
$^{65}\text{Cu}^{2+}$	0.2	-	0.1	-	0.1	0.4	90°	180° - S	60°
$^{63}\text{Cu}^{2+}$	0.4	-	0.3	-	0.5	1.3	90°	60°	180° - S
$^{65}\text{Cu}^{3+}$	-	-	-	-	-	0.3	90°	-	-
$^{63}\text{Cu}^{3+}$	-	-	-	-	-	0.8	90°	-	-
$^{12}\text{C}^{1+}$	-	-	-	-	-	-	90°	-	-
$^1\text{H}^{1+}$	-	-	-	-	-	-	-	-	-
Total	2.7	0.3	3.0	-	2.3	5.0	90°	180° - C	180° - S

Table 4.5: Tabulated values of the area under each isotope peak ($\text{V} \cdot \text{s} \cdot 10^{-6}$) at a 200 V plate bias

For the first and lowest plate bias used (50 V) one can see that the flat target plasma signals (180° – S, H, C) all have much a much higher population of lowly charged states, while the opposite is true for the narrower wedge targets. The 90° wedge angle yields the highest percentage of highly charged states, for both Cu and C. From an initial look one can observe the actual percentage distribution of isotopes in the Cu target. For natural copper the isotope distribution is ca. 70:30 of ^{63}Cu : ^{65}Cu for the majority of the recorded signals. There is no significant difference in the isotope distribution for a single Cu charged state, i.e. if one isotope is affected then the other is affected in the same way – the 70:30 split remains constant while the overall signal may change. If one Cu isotope is observed, then the corresponding isotope for that charged state will also be found in the plasma signal with the expected 70:30 distribution.

The 90° target also yields a higher H signal at each pass energy used, which is interesting as this is the only charged state for this element that is present, rather than the multiple ion states of both Cu and C. An initial assumption might be made from Cu and C ion signals that single and lowly charged states will be more prominent for only the flat targets - but this does not hold.

For every pass energy that was tested one observes a notable increase in the percentage of highly charged states as the target angle is decreased from 180° to 90°. For the 60° and 30° wedges one can see a higher population of more HCIs compared to the flat targets, but not to the same extent as plasmas for on the 90° wedge angle targets.

In addition, when summing up the total signal (area under each peak) for every target type, one can observe that the 90° target produces a significantly higher total signal for some pass energies (at a plate bias of $\Delta V = 75$ V and 100 V). The lowest total signal is generally from the 180°-H and 30° targets for each pass energy. The reason behind this is obvious for the 180°-H signal as only half of the incoming laser energy is present compared to every other signal type, meaning the plasma plume is a far less energetic. However, the 30° wedge angle produces an even lower ion signal despite having twice the incoming laser energy. This follows the trend of decreasing ion signals from 90° to 60° to 30°. At each pass energy some target configurations fail to produce any of the highly charged states of Cu and C that the 90° wedge generates. This trend becomes even more pronounced at higher pass energies.

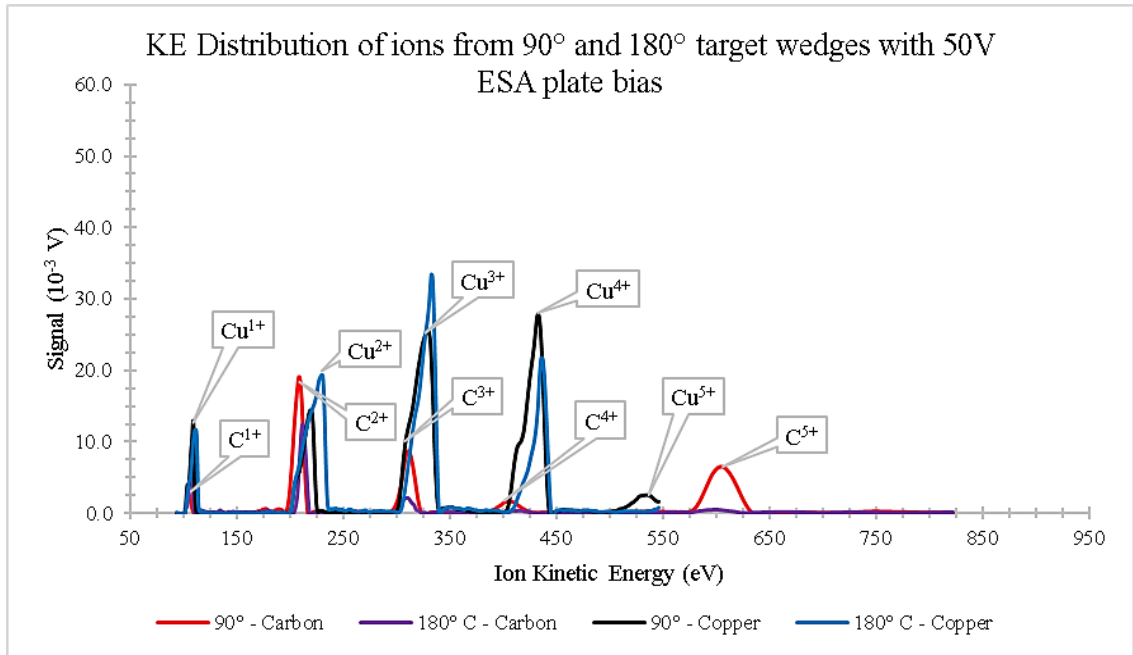


Figure 4-17: Kinetic energy distribution of ions from colliding plasmas formed on 90° and 180° wedge targets with a 50 V ESA bias

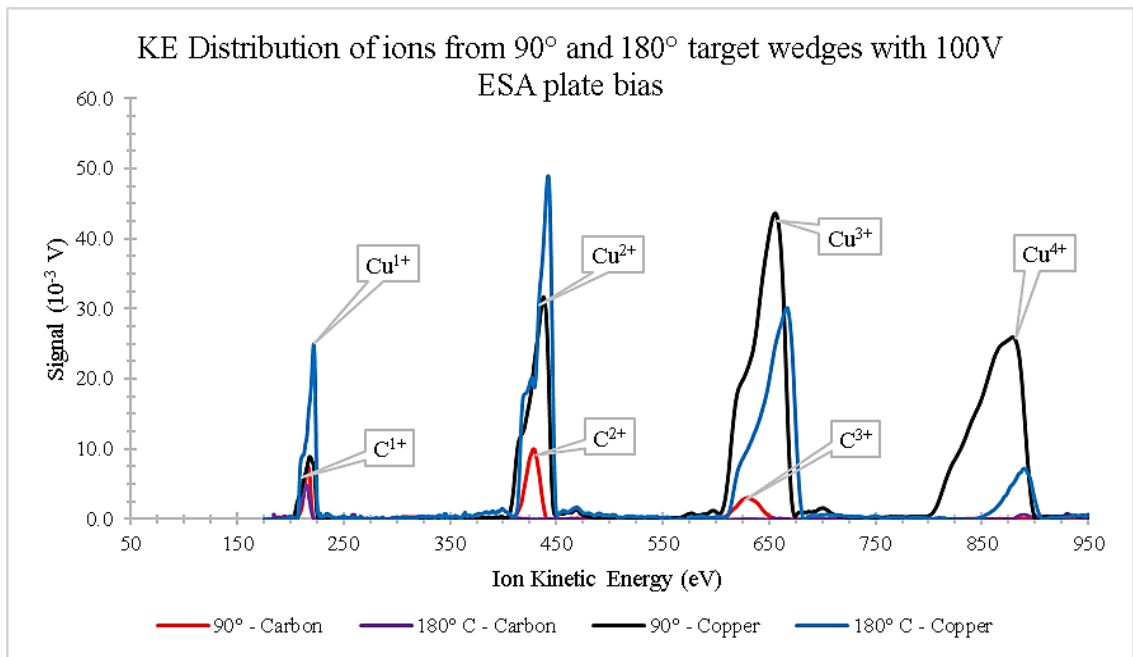


Figure 4-18: Kinetic energy distribution of ions from colliding plasmas formed on 90° and 180° wedge targets with a 100 V ESA bias

The above Figures 4.17 and 4.18 show some of the same ion signals displayed in Figures 4.7, 4.8, 4.11 and 4.12, notably the 90° and 180°- C plots. The ESA signal is shown here with respect to the kinetic energy of the ions, rather than just the ToF values of Figures 4.2 and 4.3. This offers an insight to the kinetic energy distribution of the ions measured in electronvolts, obtained simply by applying the classical

$$KE = \frac{1}{2}mv^2 \quad (4.2)$$

, where m represents the distinct ion masses (copper and carbon) and v is the ion velocity calculated from the ToF values ($velocity = distance/time$). These graphs serve to illustrate the large increase in the kinetic energy of accepted ions as the plate bias is increased from 50 to 100 V, as well as the increased total kinetic energy of the higher charged states of copper and carbon which. In Figure 4.18 in particular, for the 90° Cu ion signal one observes a 1200% increase in the total kinetic energy (the integrated area under each ion peak) of $^{63}\text{Cu}^{4+}$ ions (117×10^{-5} eV V) when compared to $^{63}\text{Cu}^{1+}$ (9.4×10^{-5} eV V). This can be compared to the 180° C target, which sees a decrease of 31% in the total kinetic energy of the higher charged states of Cu it produces ($^{63}\text{Cu}^{1+} = 20 \times 10^{-5}$ eV V, $^{63}\text{Cu}^{4+} = 14 \times 10^{-5}$ eV V). The kinetic energy measurements plotted here line up with the calculated energy values displayed in Table 3.7.

5 Discussion

5.1 Summary of Findings

From the results displayed it has been shown that one can clearly exercise varying degrees of control over the ionisation distribution of the colliding plasma stagnation layer by altering the target geometry.

Examining the ion signals produced from a single laser produced plasma vs a colliding plasma on a flat target, it is observed that at higher pass energies the colliding plasma exhibited a greater overall signal strength. At lower pass energies the ion signal from a single plasma plume was greater. So one can conclude that the stagnation layer produced by two seed plasmas will result in a greater percentage of more energetic highly charged states, a finding that corresponds with a similar experiment by P. Yeates et al [14]. It is believed that this is due to the increased number of collisions the charged particles undergo as the two seed plasmas collide and interact. More collisions also implies a greater recombination rate though, and this could explain why one observes an overall higher total signal for the single plasma plume than for that of the colliding plasma on a flat Cu target.

When the wedge targets are used there is a dramatic shift in the charge state distribution compared to the flat target plasmas. Out of the three wedges used the 90° target signal displays the most dramatic results of all. For each pass energy tested there was a notable shift in ionisation distribution towards more highly charged states, dwarfing the ion signals generated from the flat targets. At a plate bias of 75 V the signal observed for $^{12}\text{C}^{3+}$ has an integrated value of 1.56×10^{-6} for colliding plasmas on a 90° target and only 6.0×10^{-9} for a pair of plasmas formed on a flat (180°) target (where the units are Vs). This is an increase of 260 times greater for the 90° wedge over the 180° colliding plasma for this ion signal and represents an extreme case. Perhaps a more realistic example would be the $^{63}\text{Cu}^{5+}$ signal for the same plate bias, which gave values of 3.37×10^{-6} Vs for 90° and 9.1×10^{-7} Vs for 180°-C cases, an ~ 3.7 x increase for the wedge target. Further comparisons can be made from the data shown in the results section with

increases of varying amounts for different charge states, but the overall trend of a larger signal for more highly charged states from the 90° target is clear. In fact this pattern of a significant increase in more HCIs for colliding plasmas formed on a 90° wedge target compared to a flat target holds true for all plate bias values. These increases are most dramatic at lower pass energies ($\Delta V \leq 100$ V) as seen in Tables 4.1-4.3.

Compared to the flat target the 90° target angle increases the highly charged ion component for both Cu and C, as well as increasing the single H signal, but it also slightly lowers the kinetic energy of detected particles, meaning there is a greater number of highly charged states for a 90° colliding plasma, but most prominently at lower kinetic energies (pass energies). While smaller target angles do still produce an increase in the proportion of highly charged states, the effect is less for 30° and 60° targets. While relative collision velocity is still increasing, which should manifest as a greater number of more HCIs, the narrower angles appear to decrease the forward velocity component of the plasma expansion. One suspects the more highly charged states are still being generated, perhaps even to a greater extent, but they are no longer reaching the ESA. This is supported by the fact that the total signal collected from the 60° and 30° targets is far less than the 90° and 180°-C/S targets for each pass energy, despite the incoming total laser energy being equal in all cases (except for the halved laser energy case on a flat target). When one increases the relative collision velocity of the plumes the stagnation layer generated becomes “softer”, with increased levels of interpenetration between the two plumes. This softer stagnation layer and greater mean free path (mfp) means that instead of the ion signal being emitted primarily from the thin stagnation layer, there is a broader region of the plasma emitting ions. On decreasing the target wedge angle to 60° and 30° the interpenetration layer broadens and continues to emit more HCIs. The effect of having such a broad emitting region and low forward-velocity component for the expanding plasmas means that only a small amount of this signal actually ends up reaching the ESA for detection.

In summary it is proposed that the generation of highly charged states from narrow wedge targets is due to the increased relative collision velocity. This higher relative collisional velocity of the laser plasmas expanding towards each other from the wedge targets results in more energetic ions and a longer ion mfp, as well as a softer stagnation layer, with the plasmas interpenetrating to some extent (equations 2.8 and 2.9). This transfer from the kinetic energy E_k of the plumes to the ionisation mechanisms within

the stagnation layer is responsible for the resultant greater yield of more highly charged states, and the decrease in more lowly charged states of both copper and carbon ions relative to single plasma plumes.

6 Conclusions and Future Work

Ultimately this work has shown the substantial effect that target geometry can have on the ion distribution from a pair of laser produced colliding plasmas. By using narrow wedge shaped targets (especially, a 90° Cu wedge) it has been shown that one can significantly increase the percentage of more highly charged ion states compared to a similar pair of plasmas created on a flat 180° target. While the 60° and 30° wedge targets used did produce a slightly higher percentage of more HCIs, the effect was not as pronounced as in the 90° wedge case. In the particular case of colliding plasmas on a flat target vs a 90° wedge, an obvious trend could be seen when the integrated area under each ion stage was examined. By comparing the top two highest charged states of Cu for each pass energy tested, the 90° signal, on average, gave a three-fold increase in the amount of more HCIs present compared to a flat target. This was in tandem with a similar decrease in the amount of more lowly charged ions present from the 90° signal.

A large part of the work completed here involved producing the correct experimental conditions and equipment for the tests, particularly in improving the ESA resolution to acceptable levels to allow one to discriminate between the charges, their isotopes and ionisation stages. Ideally one would have liked to examine the ion signals produced from a greater variety of target types, such as wedges with angles between 180° and 90° and also different shaped targets or plasmas such as the conical ring plumes used by Cabalin et al, which were investigated for their distinct photoemissions [47].

Some brief experiments were carried out concerning the placement of magnetic fields behind the wedge targets to examine the effect that might have on the plasmas and stagnation layer, be it accelerating the ions or perhaps altering the stagnation layer formation itself. However due to time constraints it was impossible to conduct further experiments once stable well resolved signals with the ESA had been achieved. Heating and manipulating plasmas through the application of external magnetic fields is currently of significant interest [48] and could be explored in a future project.

An important facet to examine to truly round off this work would be to measure the ion signal from these targets at different angles. Instead of measuring a narrow beam of ions directly perpendicular to the target, signals should be measured at various angles in

orthogonal planes to fully characterize how the charge state distribution varies in space for all target configurations.

Others have used higher laser intensities, above 1×10^{14} W/cm², to influence the generation of more highly charged states through the nonlinear processes in the plasma [49]. The experiment herein used lower fluences of 3.8×10^9 W/cm² for the sake of higher signal resolution and system limitations, but if possible this is an area that one could explore in conjunction with wedge targets.

In this vein, there are several modifications that could still be made to further improve the ESA resolution, making the aforementioned experiments possible as well as improving the signals overall. One straightforward alteration would be a longer drift tube length, allowing the charged particles more time to spatially separate while travelling from target to detector, increasing the ToF. This is entirely dependent on the setup and laboratory space and materials available for the experiment (which were not available at the time) but is a largely trivial modification that allows the use of the increased laser fluence discussed previously. There are also changes that could be made to the detector itself by further increasing certain physical dimensions that were already investigated somewhat (specifically, by using a smaller entrance and exit slit width to reduce the range of pass energies allowed through the detector). From the ESA resolution dependencies (equation 3.7) one can see that by increasing the radial length of the curved plates it is possible to further fine-tune the charge-to-mass discrimination effect. This increases the arc length of the mean radial path r_0 that the ideal charged particle travels along, resulting in a narrower range of pass energies E_p ultimately reaching the electron multiplier. From the same ΔE equations it is clear that decreasing the slit width also improves the resolution, limiting the range of kinetic energies of ions allowed to pass.

References

- [1] D. Tabor, *Gases, liquids and solids*, Second. Cambridge: Cambridge University Press, 1979.
- [2] G. Hammett, "Introduction to Plasma Physics," Princeton, New Jersey, 2010.
- [3] I. Langmuir, *Thermionic Phenomena: The Collected Works of Irving Langmuir Volume 3*. London: Pergamon Press, 1961.
- [4] C. Sanchez-Ake, R. Sangines-de-Castro, H. Sobral, and M. Villagran-Muniz, "Plume Dynamics of Cross-Beam Pulsed Laser Ablation of Graphite," *J. Appl. Phys.*, vol. 100, no. 053305, p. 7, 2006.
- [5] T. R. Dittrich *et al.*, "Review of indirect-drive ignition design options for the National Ignition Facility Review of indirect-drive ignition design options for the National Ignition Facility *," *Phys. Plasmas*, vol. 6, no. 5, pp. 2164–2170, 1999.
- [6] R. W. Clark, J. Davis, A. L. Velikovich, and K. G. Whitney, "X-ray lasing in colliding plasmas," *Phys. Plasmas*, vol. 4, no. 10, pp. 3718–3724, 1997.
- [7] C. D. Gregory *et al.*, "Astrophysical Jet Experiments With Colliding Laser-Produced Plasmas," *Astrophys. J.*, no. 676, pp. 420–426, 2008.
- [8] P. Yeates, "A Spectroscopic and Diagnostic Study of Laser Plasma Generation and Evolution Under Multi-Variable Target Conditioning," Dublin City University, 2004.
- [9] E. Archbold, D. W. Harper, and T. P. Hughes, "Time-Resolved Spectroscopy of Laser-Generated Microplasmas," *Br. J. Appl. Phys.*, vol. 15, pp. 1321–1327, 1964.
- [10] B. C. Boland, F. E. Irons, and R. W. P. McWhirter, "A Spectroscopic Study of the Plasma Generated by a Laser from Polyethylene," *J. Phys. B At. Mol. Phys.*, vol. 2, no. 1, pp. 1180–1193, 1968.
- [11] D. Colombant and G. F. Tonon, "X-ray emission in laserproduced plasmas X-ray emission in laser-produced plasmas," vol. 3524, no. May 2013, 1973.

- [12] S. Amoruso, R. Bruzzese, N. Spinelli, and R. Velotta, “Characterization of laser-ablation plasmas,” *J. Phys. BAt. Mol. Opt. Phys.*, 1999.
- [13] J. Dardis and J. T. Costello, “Stagnation Layers at the Collision Front Between Two Laser-Induced Plasmas : A Study Using Time-Resolved Imaging and Spectroscopy,” *Spectrochim. Acta Part B*, vol. 65, no. 8, pp. 627–635, 2010.
- [14] P. Yeates, C. Fallon, E. T. Kennedy, and J. T. Costello, “Charge Resolved Electrostatic Diagnostic of Colliding Copper Laser Plasma Plumes,” *Phys. Plasmas*, vol. 18, no. 103104, pp. 1–11, 2011.
- [15] C. Fallon, P. Hayden, N. Walsh, E. T. Kennedy, and J. T. Costello, “The Effect of Wedge Angle on the Evolution of a Stagnation Layer in a Colliding Plasma Experiment,” *J. Phys. Conf. Ser.*, vol. 548, pp. 1–7, 2014.
- [16] C. Fallon, “Optical Diagnostics of Colliding Laser Produced Plasmas : Towards Next Generation Plasma Light Sources,” Dublin City University, 2013.
- [17] J. D. Gillaspay, J. M. Pomeroy, A. C. Perella, and H. Grube, “The Potential of Highly Charged Ions : Possible Future Applications,” *J. Pphysics Conf. Ser.*, vol. 13, pp. 451–456, 2007.
- [18] U. Amaldi and G. Kraft, “Reports on Progress in Physics Related content Radiotherapy with beams of carbon ions,” *Reports Prog. Phys.*, vol. 68, pp. 1861–1882, 2005.
- [19] P. Hough, C. Mcloughlin, S. S. Harilal, J. P. Mosnier, and J. T. Costello, “Emission characteristics and dynamics of the stagnation layer in colliding laser produced plasmas,” pp. 2–7, 2010.
- [20] K. F. Al-Shboul *et al.*, “Interpenetration and Stagnation in Colliding Laser Plasmas,” *Phys. Plasmas*, vol. 21, no. 013502, pp. 1–8, 2014.
- [21] W. C. Wiley and I. H. McLaren, “Time of Flight Mass Spectrometer with Improved Resolution,” *Rev. Sci. Instrum.*, vol. 26, no. 12, pp. 1150–1157, 1955.
- [22] K. Dolder and B. Peart, “Experimental Aspects of Two-Body Ion-Ion Collisions,” *Reports Prog. Phys.*, vol. 48, pp. 1283–1332, 1985.
- [23] N. Walsh, “Laser Produced Plasmas in Liquid Environments,” Dublin City

University, 2016.

- [24] J. Reif, *Laser-Surface Interactions for New Materials Production Tailoring Structure and Properties*. 2010.
- [25] B. Doggett, “Characterisation of Laser Produced Plasmas,” University of Dublin Trinity College, 2006.
- [26] J. R. Ho, C. P. Grigoropoulos, and J. A. C. Humphrey, “Gas dynamics and radiation heat transfer in the vapor plume produced by pulsed laser irradiation of aluminum Gas dynamics and radiation heat transfer in the vapor plume produced by pulsed laser irradiation of aluminum,” vol. 7205, 1996.
- [27] M. Kelly, “Ultrafast and Intense Laser Interaction with Gases and Solids,” Dublin City University, 2013.
- [28] W. D. Hayes and R. F. Probstein, *Physics of Shock Waves and High-Temperature Hydrodynamic Phenomena*. New York: Elsevier, 1967.
- [29] L. Spitzer, *Physics of Fully Ionized Gases*. New York: Dover Publications, 1956.
- [30] A. Caruso and R. Gratton, “Some properties of the plasmas produced by irradiating light solids by laser pulses,” *Plasma Phys.*, vol. 10, pp. 867–877, 1968.
- [31] P. Hough *et al.*, “Ion Emission in Collisions Between Two Laser-Produced Plasmas,” *J. Phys. D. Appl. Phys.*, vol. 44, pp. 1–4, 2011.
- [32] P. W. Rambo and J. Denavit, “Interpenetration and ion separation in colliding plasmas Interpenetration and ion separation in colliding plasmas,” *Phys. Plasmas*, vol. 4050, no. 1994, pp. 4050–4060, 2014.
- [33] C. Chenais-Popovics *et al.*, “Kinetic to thermal energy transfer and interpenetration in the collision of laser-produced plasmas,” *Phys. Plasmas*, vol. 4, no. May 2013, pp. 190–208, 1997.
- [34] D. Feldbaum, N. V Morrow, S. K. Dutta, and G. Raithel, “Coulomb Expansion of Laser-Excited Ion Plasmas,” pp. 1–4, 2002.
- [35] Analytical West, “Analytical West Electron Multiplier Small Horn Plug-in,” 2009. [Online]. Available: <https://www.analyticalwest.com/em-2300.html>. [Accessed:

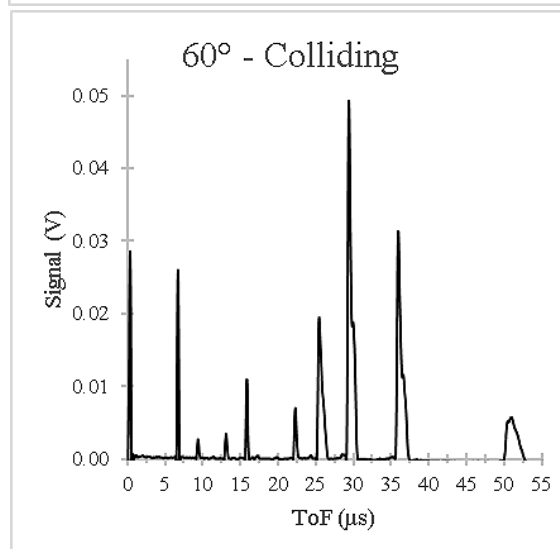
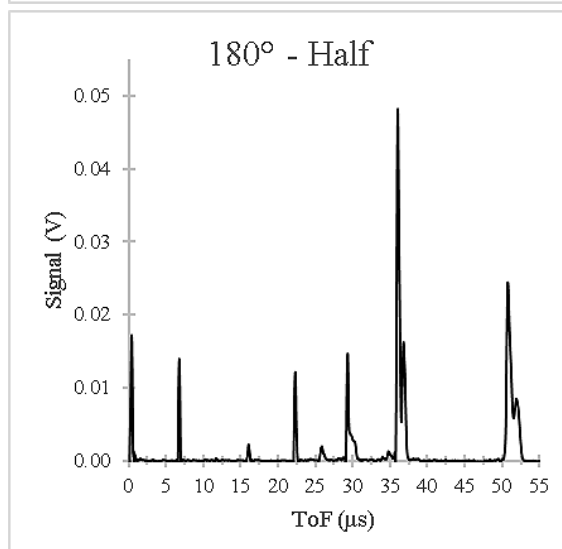
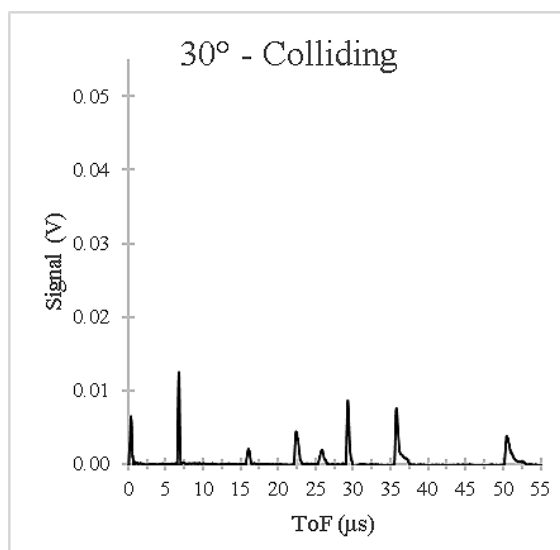
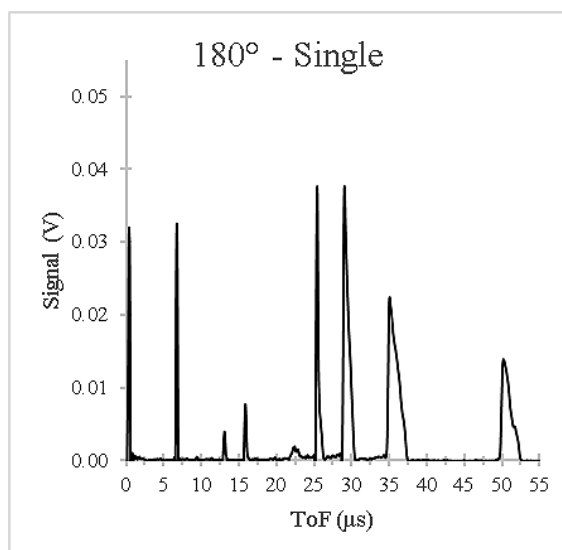
12-Jul-2018].

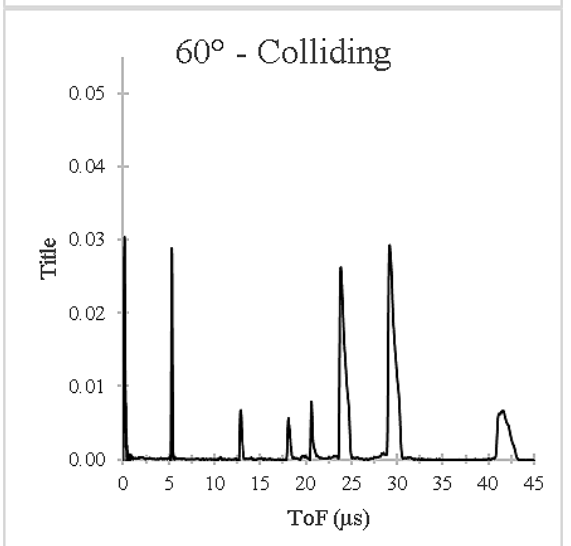
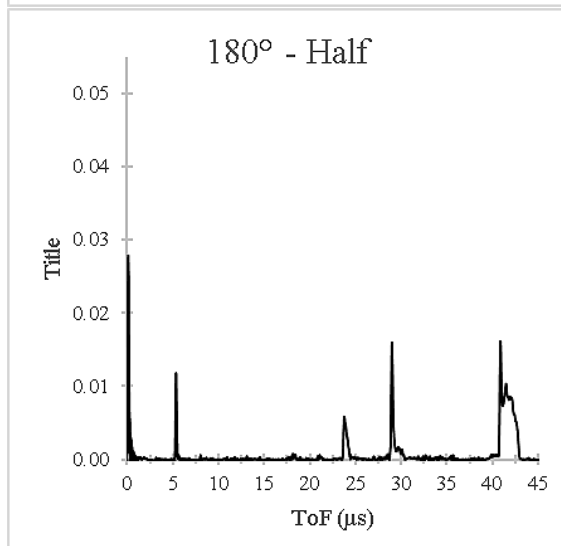
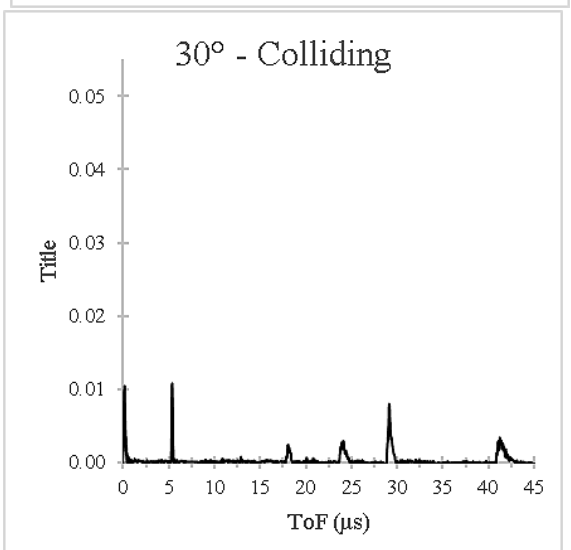
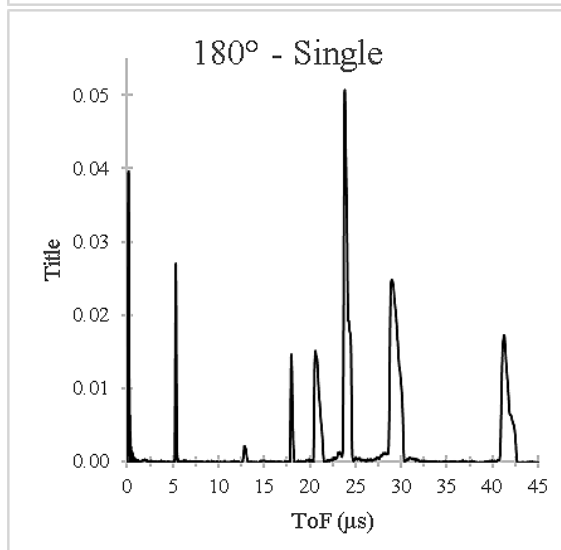
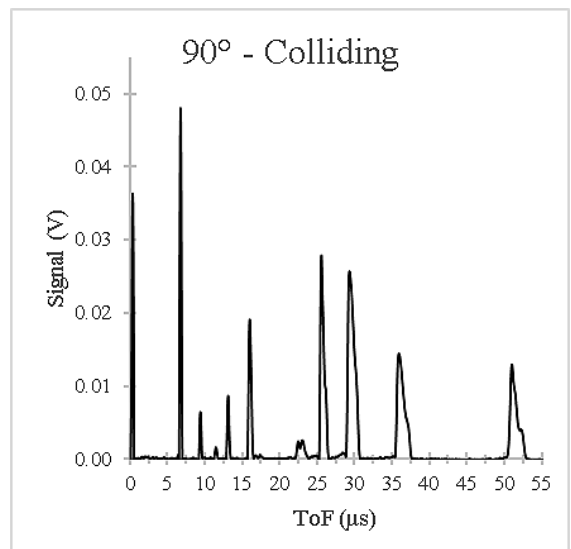
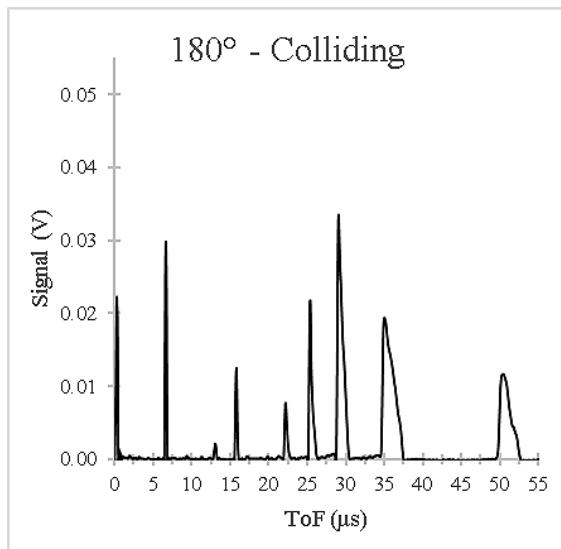
- [36] M. Rahman, A. S. Kumar, and J. R. S. Prakash, "Micro milling of pure copper," vol. 116, pp. 39–43, 2001.
- [37] E. Song, "The Machinability of Pure Copper," *Linkedin*, 2017. [Online]. Available: <https://www.linkedin.com/pulse/machinability-pure-copper-edward-song>. [Accessed: 02-Jul-2018].
- [38] P. Mulser, G. Alber, and M. Murakami, "Revision of the Coulomb Logarithm in the Ideal Plasma," Darmstadt, 2014.
- [39] Newport Corporation, "Application Note: Variable Attenuator for Lasers," 2006.
- [40] E. M. Purcell, "The Focussing of Charged Particles by a Spherical Condenser," *Phys. Rev.*, vol. 54, no. November, p. 9, 1938.
- [41] O. Morris *et al.*, "Determination of Charge State, Energy and Angular Distributions of Tin Ions Emitted from Laser Produced Plasma Base EUV Sources," in *13th International Conference on the Physics of Highly Charged Ions*, 2006, pp. 1–31.
- [42] O. Morris, "Angle-resolved studies of tin laser plasma extreme ultraviolet sources .," University College Dublin, 2008.
- [43] O. Morris *et al.*, "Determination of Charge State, Energy and Angular Distributions of Tin Ions Emitted from Laser Produced Plasma Based EUV Sources," *J. Phys. Conf. Ser.*, vol. 58, pp. 391–394, 2007.
- [44] M. Brandstätter, N. Gambino, and R. S. Abhari, "Temporally and spatially resolved ion dynamics of droplet-based laser-produced tin plasmas in lateral expansion direction," *J. Appl. Phys.*, vol. 043308, no. 123, 2018.
- [45] R. W. Schafer, "What Is a Savitzky-Golay Filter?," *IEEE Signal Process. Mag.*, no. July, pp. 111–117, 2011.
- [46] Fityk, "Fityk curve fitting and data analysis," 2016. [Online]. Available: <http://fityk.nieto.pl/>. [Accessed: 12-Jul-2018].
- [47] L. M. Cabalin and J. J. Laserna, "Atomic emission spectroscopy of laser-induced plasmas generated with an annular-shaped laser beam {"}, " *J. Analytical At.*

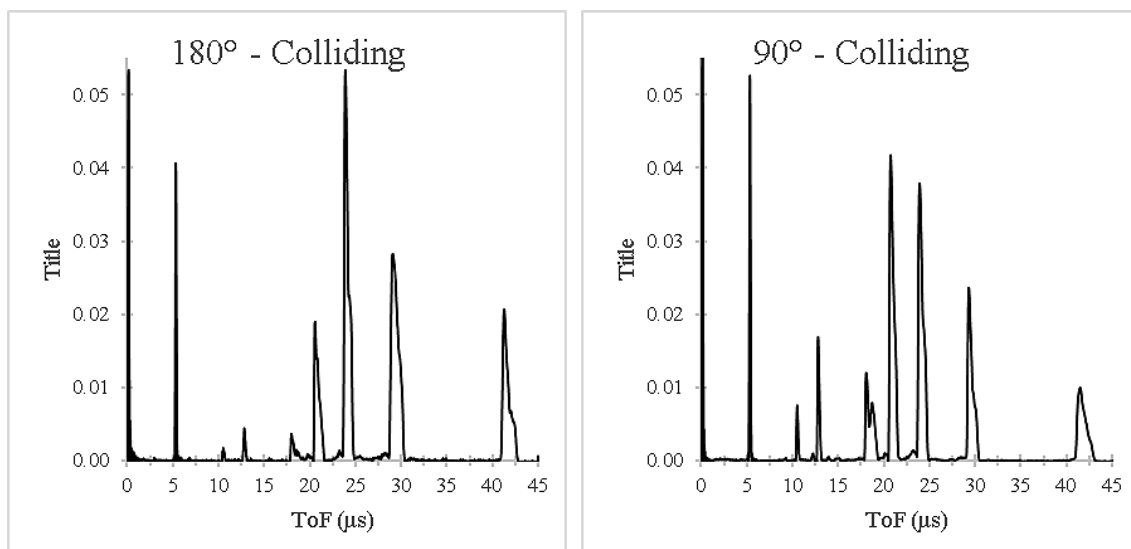
Spectrom., vol. 19, pp. 445–450, 2004.

- [48] J. R. Creel, “Heating and Compression of Laser Produced Plasmas Using Pulsed Magnetic Fields,” Trinity College Dublin, 2017.
- [49] L. Láska *et al.*, “Charge-State and Energy Enhancement of Laser-Produced Ions Due to Nonlinear Processes in Preformed Plasma,” *Appl. Phys. Lett.*, vol. 86, no. 081502, pp. 2–5, 2005.
- [50] ElfQrin, “Physics matter state transition 1 en.svg.” Wikimedia Commons, p. 0, 2011.

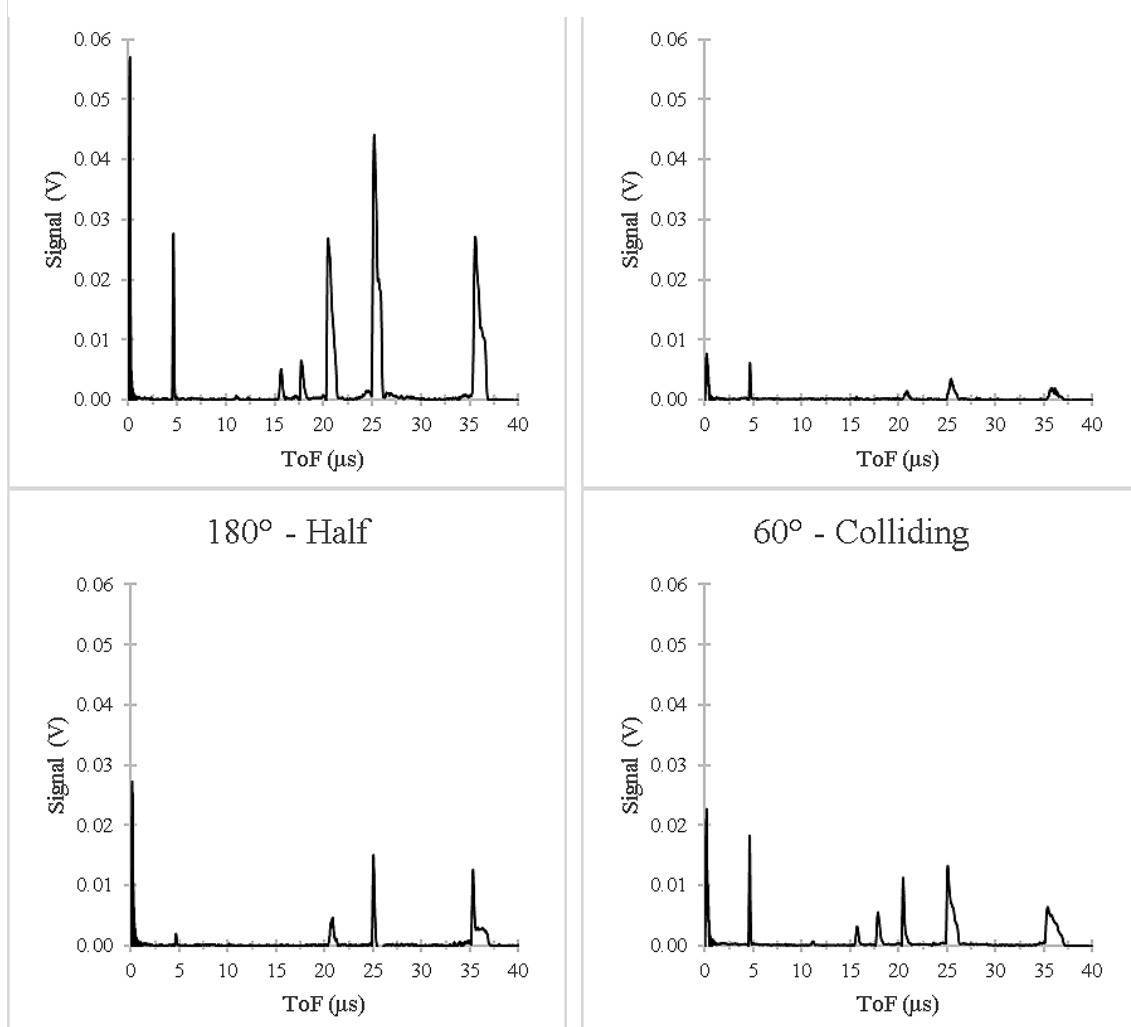
Appendix

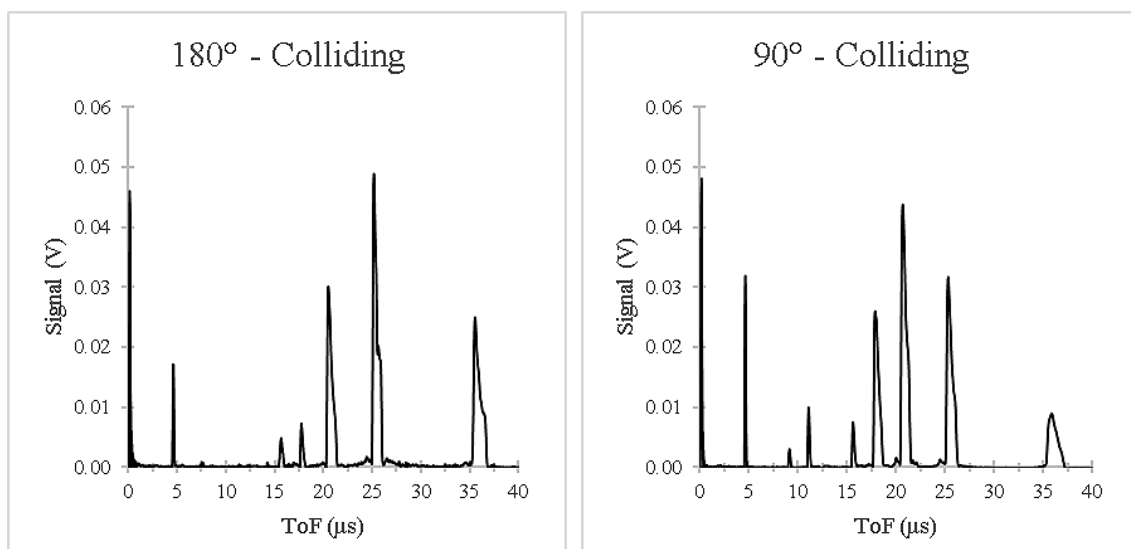




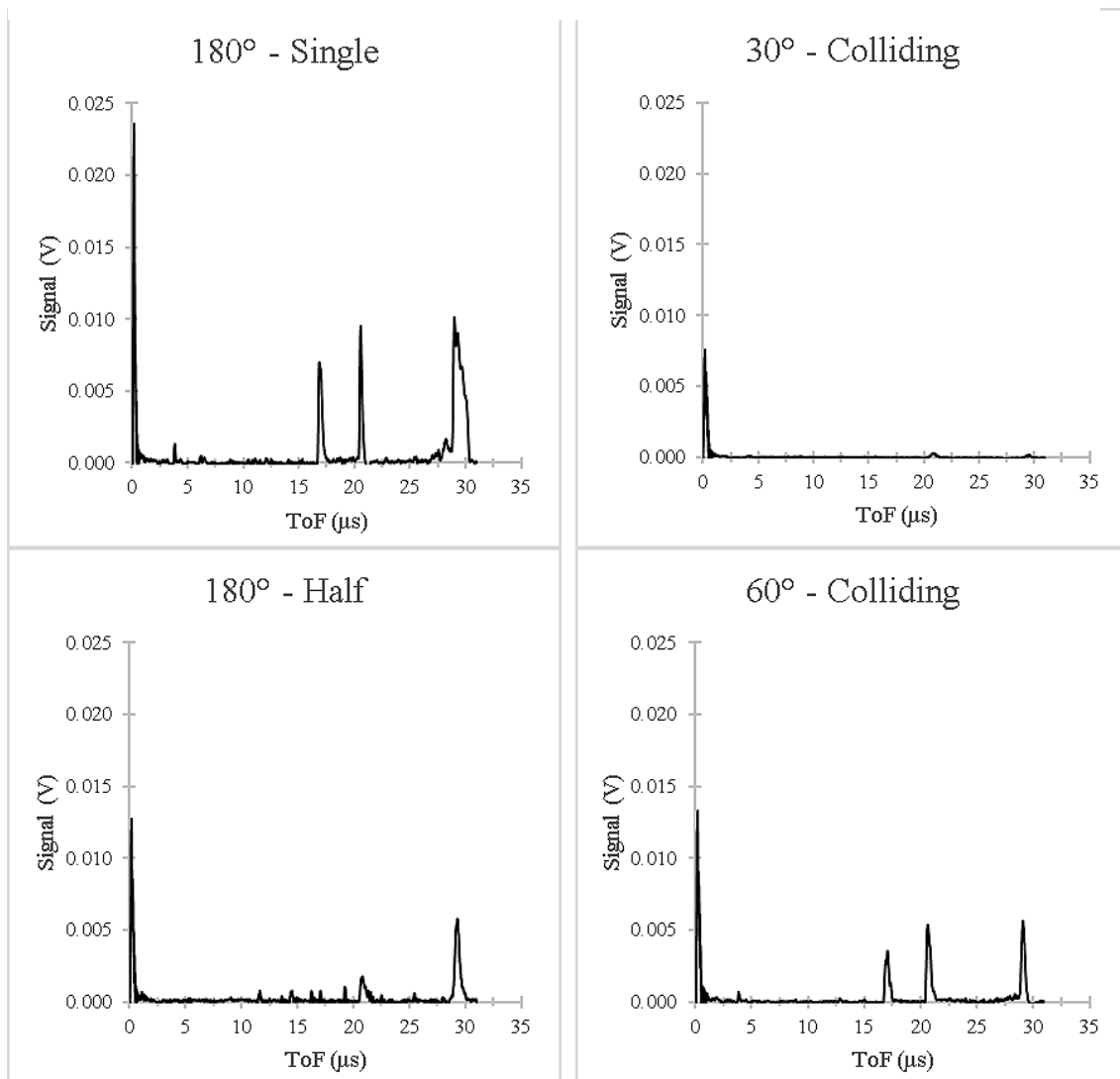


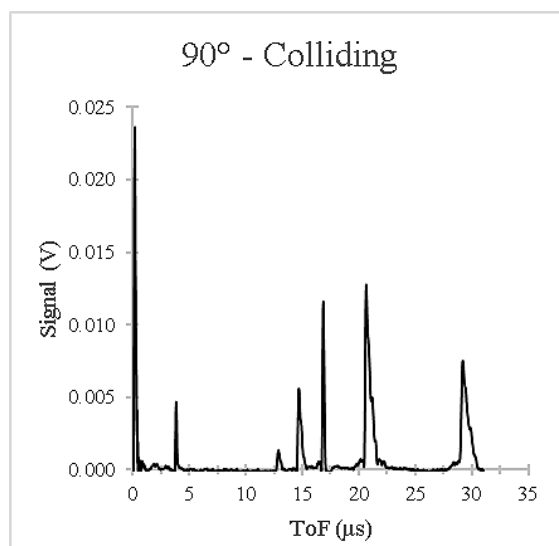
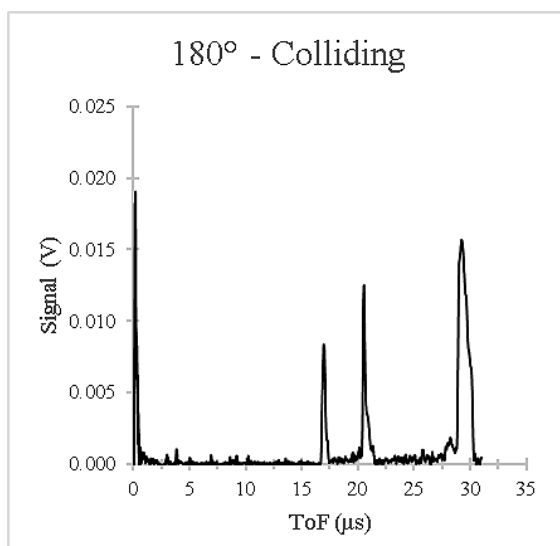
Appendix Figure 2: ESA-ToF mass spectrometry measurements at 75 V plate bias



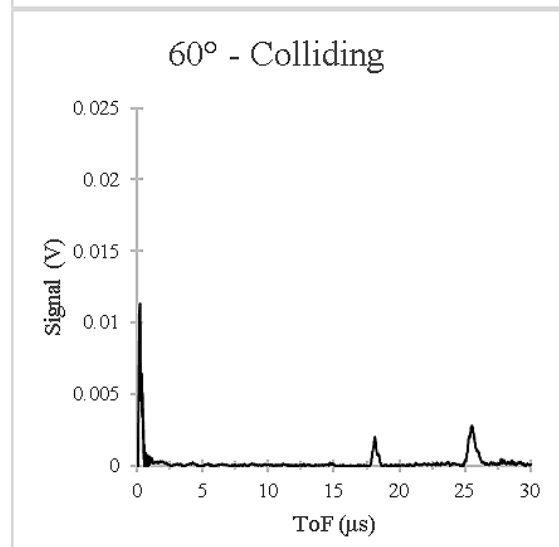
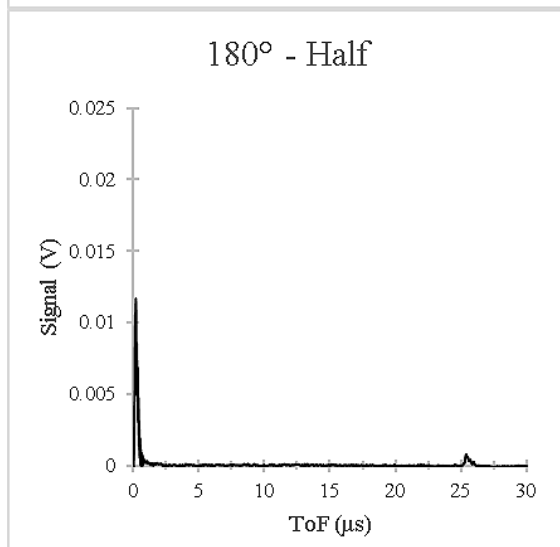
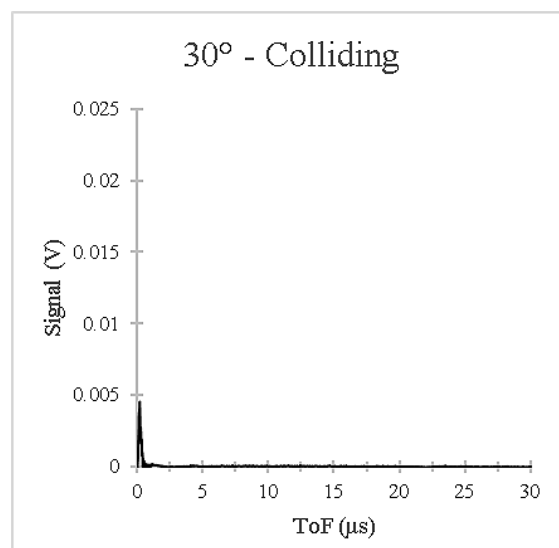
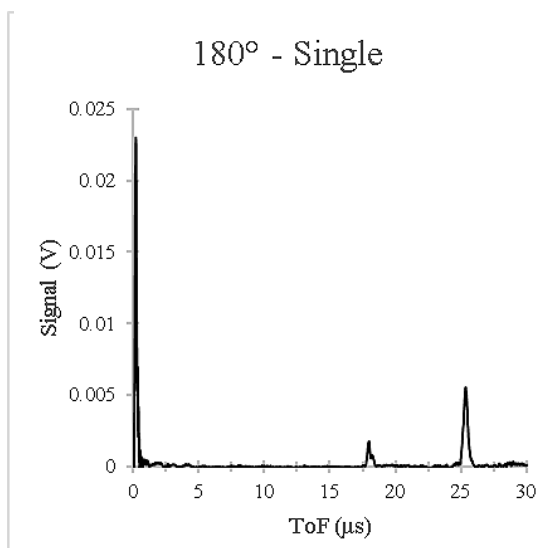


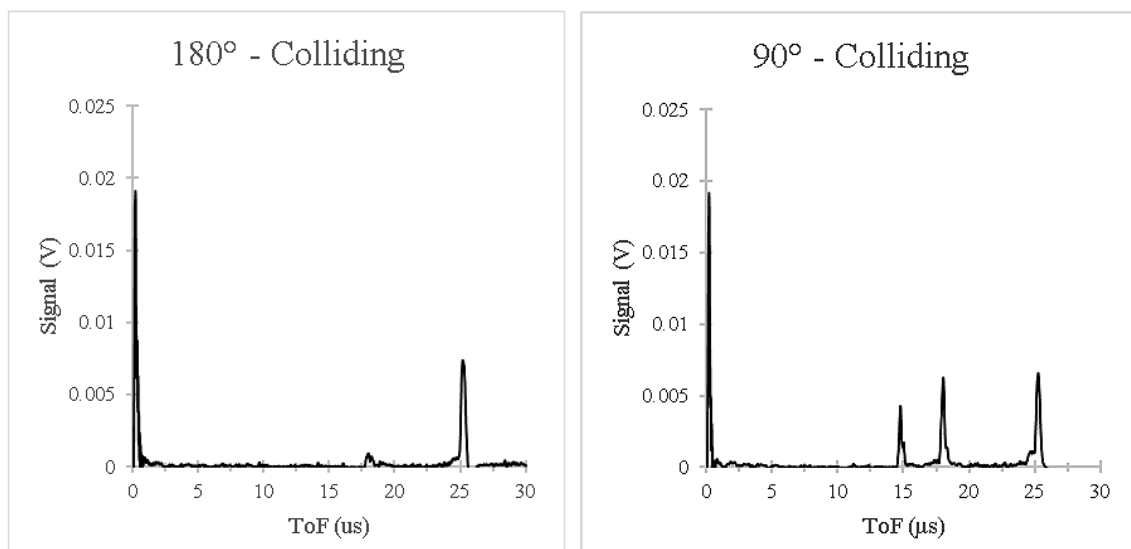
Appendix Figure 3: ESA-ToF mass spectrometry measurements at 100 V plate bias





Appendix Figure 4: ESA-ToF mass spectrometry measurements at 150 V plate bias





Appendix Figure 5: ESA-ToF mass spectrometry measurements at 200 V plate bias